The Astrophysical Journal Supplement Series, 169:439–457, 2007 April

SEMIEMPIRICAL MODELS OF SOLAR MAGNETIC STRUCTURES

H. Socas-Navarro
High Altitude Observatory, National Center for Atmospheric Research,[1] Boulder, CO; navarro@ucar.edu
Received 2006 May 22; accepted 2006 September 27

ABSTRACT

This paper presents semiempirical models of various solar magnetic structures, extending from the photosphere to the chromosphere. The models have been derived from non-LTE inversions of high-resolution spectropolarimetric observations of four Ca II and Fe I lines. The observed targets are dark and bright components of a sunspot umbra; dark and bright components of a sunspot penumbra; a canopy between two sunspots; a facula; and a network element. These models may be employed, e.g., to compute realistic synthetic Stokes spectra of photospheric and chromospheric lines.

Subject headings: line: profiles — Sun: atmosphere — Sun: chromosphere — Sun: magnetic fields

Online material: machine-readable tables

1. INTRODUCTION

Semiempirical models (i.e., those derived by fitting observed spectral features) of the quiet Sun and several magnetic structures have been available for decades now. Some of these models are based on intensity observations and do not include the magnetic field. Some of the most popular are those of Gingerich et al. (1971), Vernazza et al. (1981), Maltby et al. (1986), and Fontenla et al. (1990). Others have been obtained more recently from polarimetric observations and provide the magnetic field but do not extend into the chromosphere. Examples are the models of Collados et al. (1994) and Bellot Rubio et al. (1997).

A full multilevel non-LTE calculation with polarization induced by the magnetic field would represent an enormous undertaking, especially considering that the inversion process requires a large number of spectral syntheses as the model atmosphere is iteratively adjusted to fit the observed data. This is probably the reason that magnetic chromosphere models have not been derived in the past (with the only exception of Socas-Navarro et al. 2000a). Fortunately, it has been shown (Socas-Navarro et al. 2000b) that with some simplifying assumptions the problem becomes tractable.

Most of these assumptions work well in many realistic scenarios. For instance, the field-free approximation is valid when the magnetic splitting is much smaller than the Doppler width of the lines, which is often the case. Effects of atomic polarization (orientation and alignment) are important near the limb but can usually be neglected on the disk. Perhaps the most questionable assumption is that of hydrostatic equilibrium, but this is only used to compute gas densities and is not very important in obtaining the semiempirical stratification of physical parameters on an optical depth scale. It may be important, however, in converting the optical depths to a geometrical height scale.

2. OBSERVATIONS AND DATA ANALYSIS

The observations used in this work were acquired with the new Spectro-Polarimeter for Infrared and Optical Regions (SPINOR; Socas-Navarro et al. 2006) on 2004 June 16. The data set includes two chromospheric lines of the Ca II infrared triplet at 849.8 and 854.2 nm, recorded by two different cameras, as well as two nearby Fe I lines at 849.7 and 853.8 nm. A scan of active region NOAA 0634 was conducted starting at 15 : 16 UT. The scanning step is of $0.22''$, while the sampling along the slit direction is of $0.35''$. This active region was located at 11° latitude north and 33° longitude east during the observations.

The seeing conditions were near optimal at the time, and we employed the new high-order adaptive optics system of the Dunn Solar Telescope (Ren et al. 2003). This resulted in a spatial resolution of $\simeq 0.7''$, measured as the size of the smallest magnetic elements resolved in the magnetogram of Figures 1 and 2, which is an excellent value for this kind of observations. For example, it is possible to resolve the bright component (clusters of umbral dots) and dark cores in the umbra of the large sunspot. Some umbral dots might be nearly resolved, although most have considerably smaller sizes. In any case, the bright and dark components can be inverted separately at this resolution, allowing us to hint at the intrinsic differences between them (the real differences would obviously be larger due to the limited spatial resolution). A similar argument could be made about the penumbral filaments. Although the filaments are unresolved, we can at least separate clearly a bright and dark component.

After correcting for bias level and flat field, the data were decontaminated of instrumental polarization by applying the inverse of the polarimeter response and the telescope Mueller matrices (previously obtained from calibration operations), as explained in Socas-Navarro et al. (2006).

I selected seven different spatial locations in the map (see Table 1) for detailed inversion. In addition to two umbral and penumbral components, there is a network element, a facula, and the canopy between the two sunspots. The inversions consider a magnetic atmosphere and a stray light profile, which can also represent a (prescribed) nonmagnetic surrounding atmosphere. In this manner, the stray light fraction may be interpreted in terms of a magnetic filling factor as well. The spectral profile for stray light is determined as the average along the slit direction.

Each inversion comprises three different cycles in which the degrees of freedom are gradually increased. The numbers of nodes used for each physical parameter are listed in Table 2. During the first cycle, all Stokes profiles are weighted equally. In the second and third cycles, the Stokes Q, U, and V profiles are given 20 times more weight than Stokes I. In addition, each inversion is repeated 10 times with randomized initializations to estimate the range

[1] The National Center for Atmospheric Research (NCAR) is sponsored by the National Science Foundation.

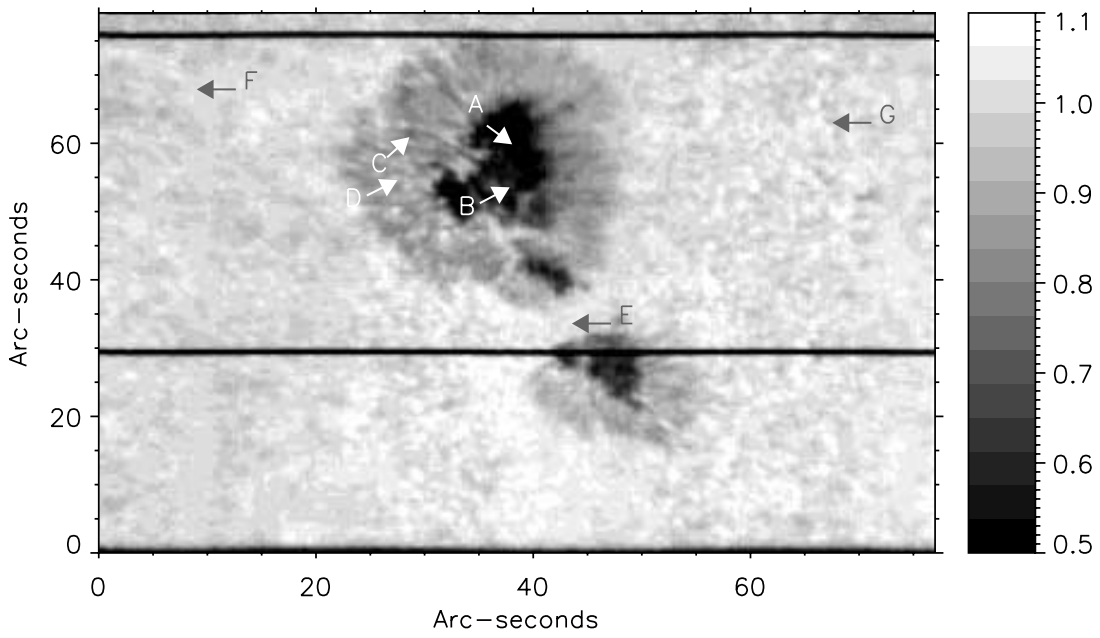

FIG. 1.—Continuum intensity map of the observed active region NOAA 0634. The arrows mark the spatial locations of the profiles inverted. East is to the left of the figure, and west is to the right. Disk center is toward the right.

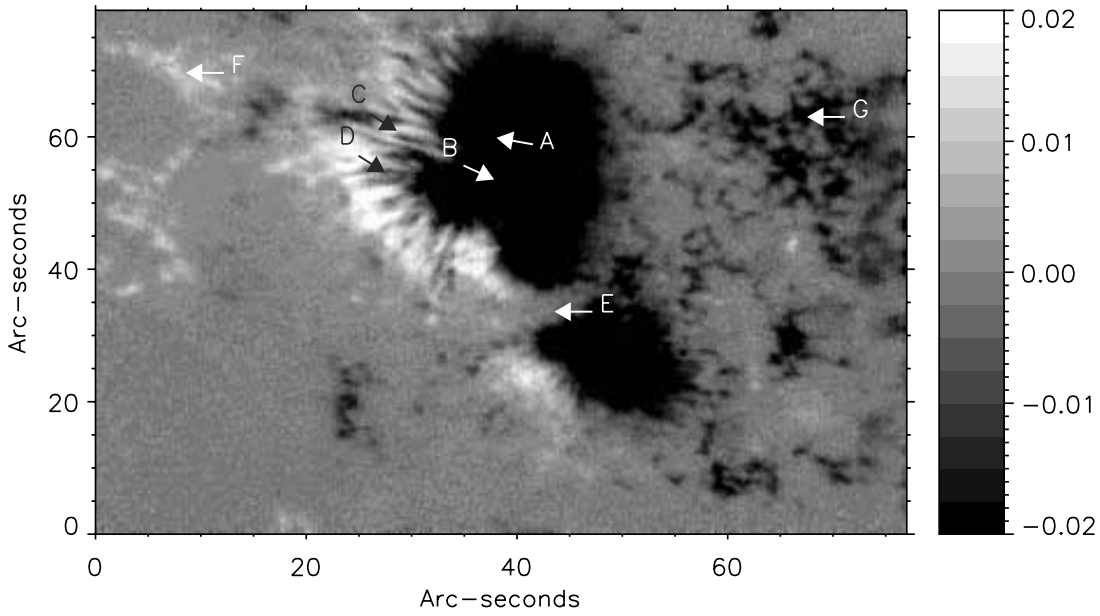

FIG. 2.—Photospheric magnetogram of the observed active region NOAA 0634. The map has been obtained by integrating the profile of Stokes *V*/*I* over a bandwidth of 10 spectral pixels (0.025 nm) on the red lobe of the 849.7 nm line.

TABLE 1
POINTS INVERTED

Label	Solar Structure	x (pixel)	y (pixel)	Relative Intensity (Continuum)
Point A	Dark umbra	172	171	0.464
Point B	Bright umbra	171	153	0.615
Point C	Dark penumbra	129	174	0.742
Point D	Bright penumbra	124	156	0.951
Point E	Canopy	197	96	1.058
Point F	Network	40	194	1.005
Point G	Facula	306	180	0.954

of models compatible with the observations. The models presented in the following section are the average of these multiple solutions, and the uncertainty region is given by their standard deviation.

Sometimes the models obtained exhibit an awkward behavior within the error bars that is difficult to understand from a physical point of view. For example, one might find a temperature that decreases inward below the $\tau_{500} = 1$ level. This may happen in layers where there is very low or no sensitivity to the physical parameters. In those situations, I have edited the models manually in order to change the atmospheric stratification to something more physically sensible (but always within the error bars of the inversion).

The model atom used for the non-LTE computations is a six-level model of Ca II, including the continuum. Collisional rates are those provided by the code MULTI of Scharmer & Carlsson (1985). The two Fe I lines are computed assuming LTE level populations, but taking into account the blends with the wings of the Ca II lines. The atomic parameters employed (rest wavelength, lower level energy, oscillator strength, and quantum numbers) are listed in Table 3. Background opacities are obtained with the opacity package used by Shchukina & Trujillo Bueno (2001).

The inversion code is essentially the same that was extensively tested in Socas-Navarro et al. (2000b) with the addition of the stray light fraction parameter. To ensure that this new parameter does not introduce instabilities in the inversion, a similar test has been performed here. I took each one of the models obtained for points A to G and synthesized a "reference" set of profiles. These reference profiles were inverted 10 times each with random initializations. The average and the standard deviation of the resulting chromospheric field strengths [defined as the median from $\log(\tau_{500}) = -4$ to -6] and the percentage of stray light (s) are shown in Table 4.[2] This test shows that the recovery is overall satisfactory, and only point F exhibits a relatively large spread in the average chromospheric field strength.

[2] Inversions in which the algorithm did not converge (as determined by large values of the χ^2 merit function) have been excluded from the statistics, but these represent only 7 out of the 70 experiments.

TABLE 2
INVERSION NODES

Parameter	Cycle 1	Cycle 2	Cycle 3
Temperature	6	11	21
Microturbulence	0	3	3
Magnetic field strength	1	1	6
Magnetic field inclination (γ)	1	1	6
Magnetic field azimuth	1	1	6
Line-of-sight velocity ($v_{\rm los}$)	2	6	11
Stray light fraction	1	1	1
Macroturbulence	0	1	1

TABLE 3
ATOMIC LINE PARAMETERS

Element	Wavelength (nm)	$E_{\rm low}$ (eV)	$\log(gf)$	$s_{\rm low}$	$L_{\rm low}$	$J_{\rm low}$	$s_{\rm up}$	$L_{\rm up}$	$J_{\rm up}$
Fe I	849.698	4.60	−0.950	1	3	3	1	3	2
Ca II	849.802	1.69	−1.318	1/2	2	1.5	1/2	1	1.5
Fe I	853.801	4.91	−1.400	2	2	4	3	4	4
Ca II	854.209	1.70	−0.363	1/2	2	2.5	1/2	1	1.5

3. RESULTS

This section is a compilation of plots and tables of the various models (Figs. 3–16 and Tables 5–11). The sign of the line-of-sight velocity is defined following the usual astrophysical convention, in which negative (positive) velocities are toward (away from) the observer. For convenience, the tables have been made publicly available in electronic format as well.[3]

The models obtained here are reliable only within a certain range of heights, approximately between $\log(\tau_{500}) = -6$ and 0 (see the shaded area in Figs. 4–16). The radiative transfer calculations, however, need to be performed in a range of optical depths somewhat broader than where the lines are formed to ensure that all transitions involved become optically thin (thick) at the top (bottom) of the atmosphere.

As a sanity check, I compared the longitudinal magnetic flux in the models to the prediction of the center-of-gravity method (Rees & Semel 1979). To the author's best knowledge, the validity of this method has not yet been explored for chromospheric lines with multilobe structure and emission reversals. Figure 17 shows a scatter plot with a rudimentary calibration of this method. To obtain this figure, many different sets of profiles were synthesized with varying temperatures, velocities, magnetic field strengths, and orientations. The center of gravity of these synthetic profiles is then compared to the "true" longitudinal magnetic flux. As one would expect, there is a certain amount of scatter, but the agreement between both quantities is in general reasonably good. Table 12 compares the result of applying the center-of-gravity method to the observed profiles and the longitudinal flux obtained in the inversions. The largest discrepancies are seen in the penumbral points, especially point C. Points C and D are both located on the limb side of the penumbra, where opposite observer-frame polarities exist along the line of sight. It seems plausible that the combination of such apparent opposite polarities result in the

[3] See http://www.hao.ucar.edu/Public/materials/ApJS_MS65396/.

TABLE 4
NUMERICAL TESTS

Point	$\langle s \rangle$	$\sigma(s)$	$\langle \lvert B \rvert \rangle$ (G)	$\sigma(\lvert B \rvert)$ (G)
A	7.28	2.58	1490.01	134.65
B	7.41	1.51	1953.95	112.436
C	22.55	1.38	726.35	35.7341
D	26.69	1.74	1202.64	86.7865
E	43.03	4.69	654.13	214.44
F	54.62	0.06	885.71	56.61
G	28.89	1.26	1266.96	135.24

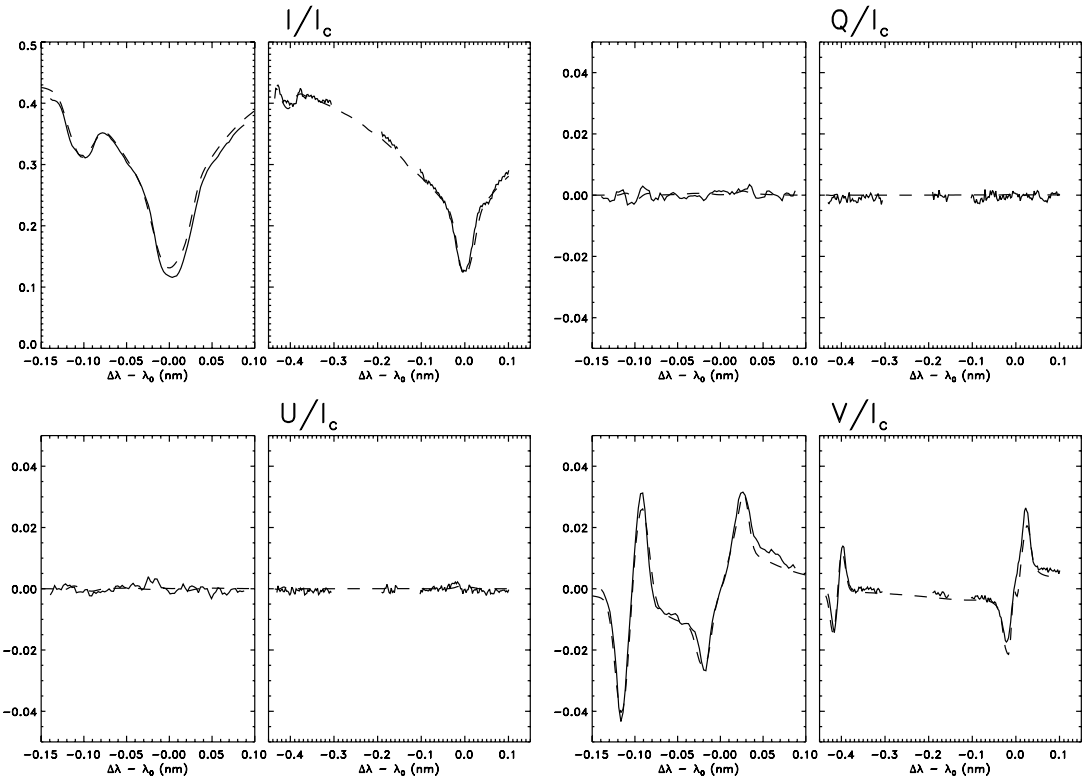

FIG. 3.—Point A: Observed (*solid line*) and synthetic (*dashed line*) Stokes profiles obtained from the fit, in units of the average quiet-Sun continuum intensity.

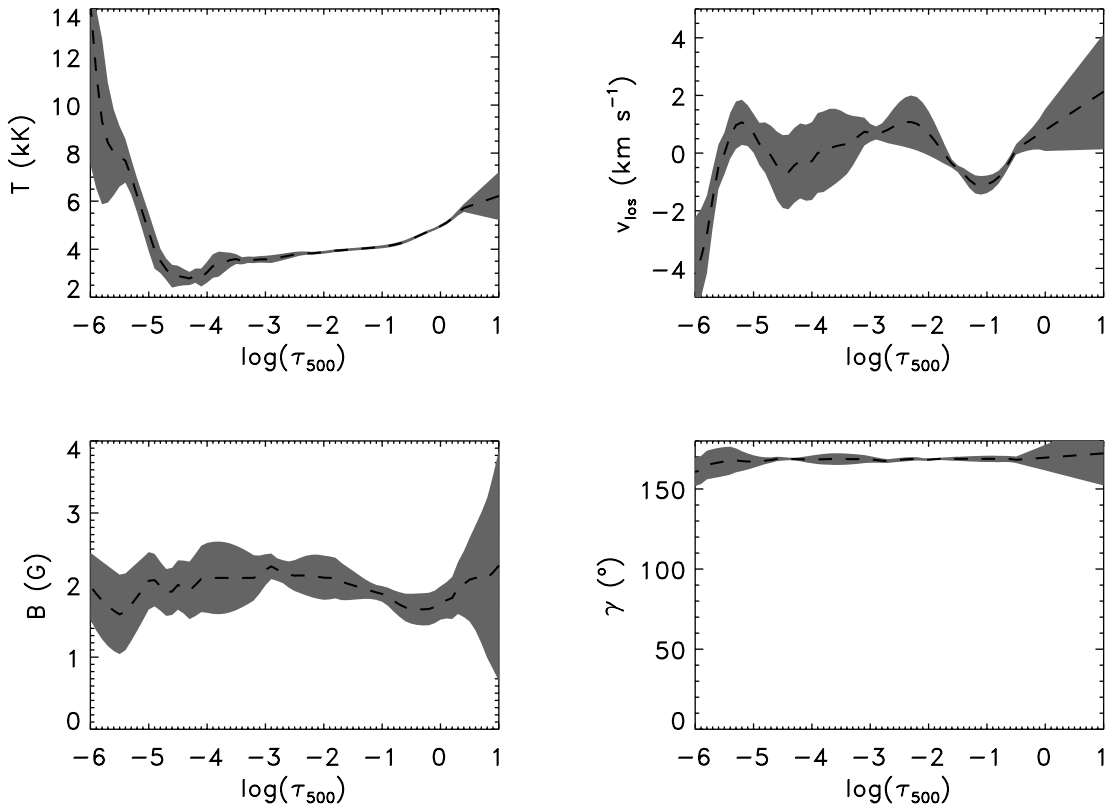

FIG. 4.—Point A: Average atmospheric stratification of temperature, line-of-sight velocity, magnetic field strength, and inclination away from the solar vertical. The shaded area represents the uncertainty.

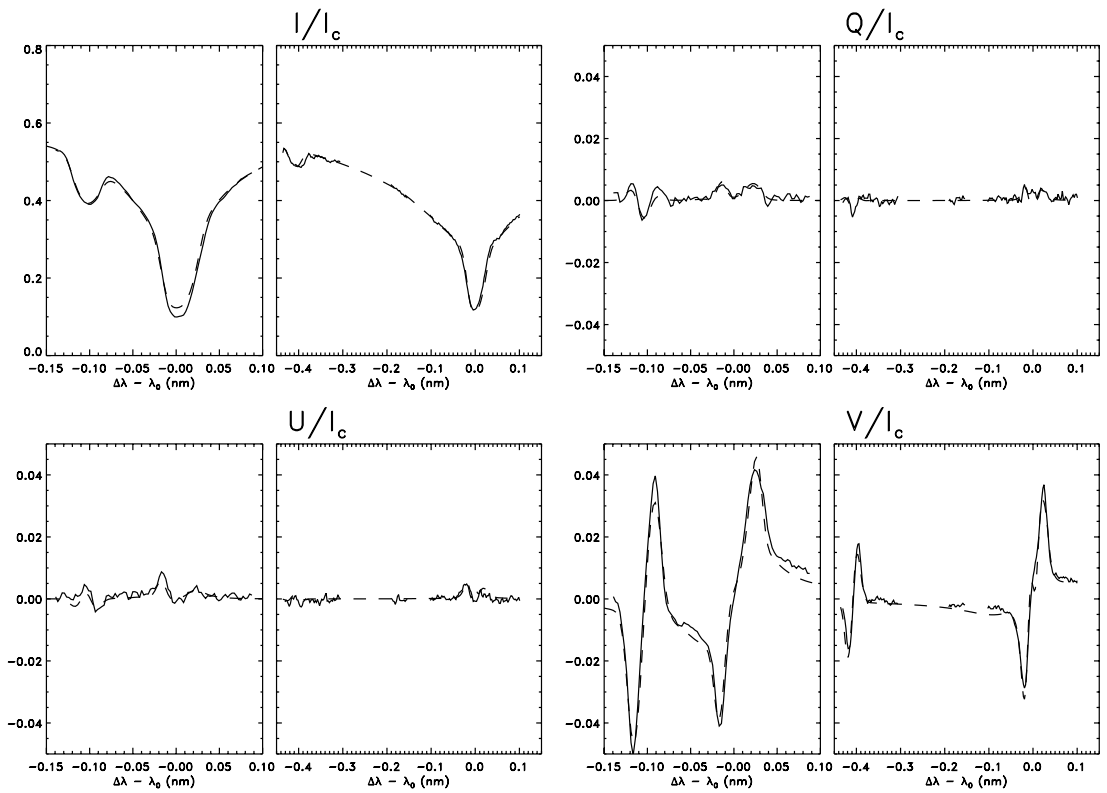

FIG. 5.—Point B: Observed (*solid line*) and synthetic (*dashed line*) Stokes profiles obtained from the fit, in units of the average quiet-Sun continuum intensity.

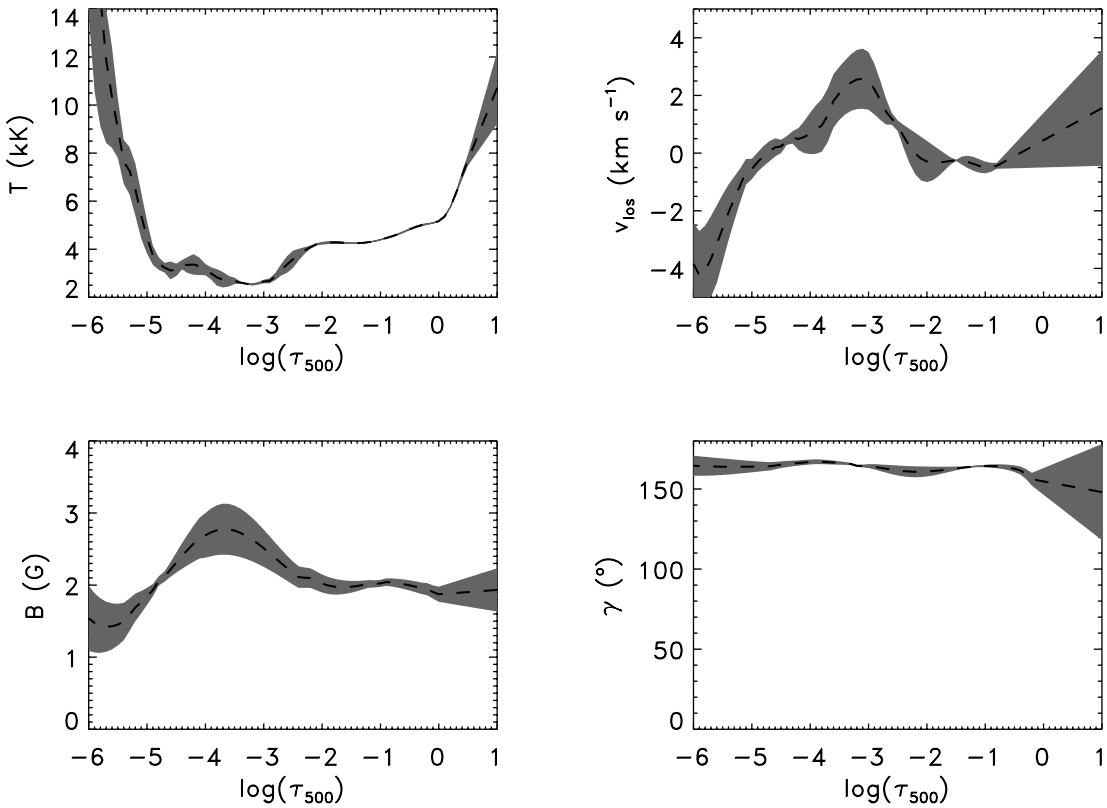

FIG. 6.—Point B: Average atmospheric stratification of temperature, line-of-sight velocity, magnetic field strength, and inclination away from the solar vertical. The shaded area represents the uncertainty.

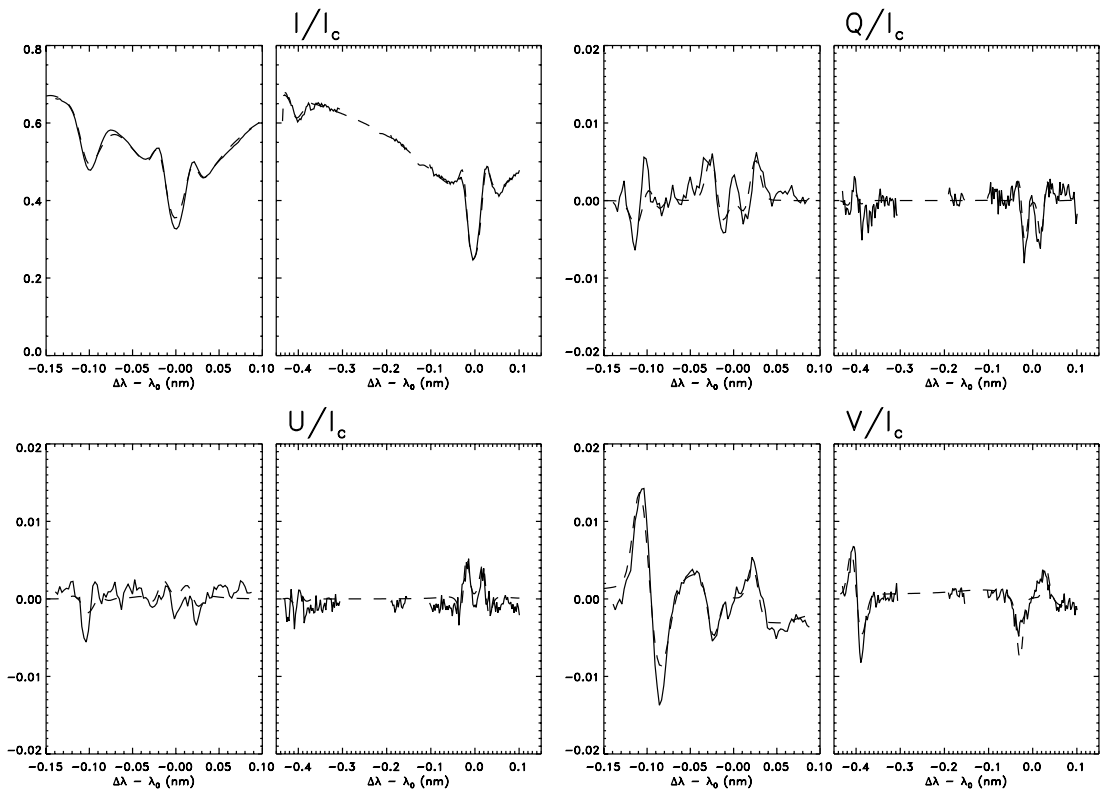

FIG. 7.—Point C: Observed (*solid line*) and synthetic (*dashed line*) Stokes profiles obtained from the fit, in units of the average quiet-Sun continuum intensity.

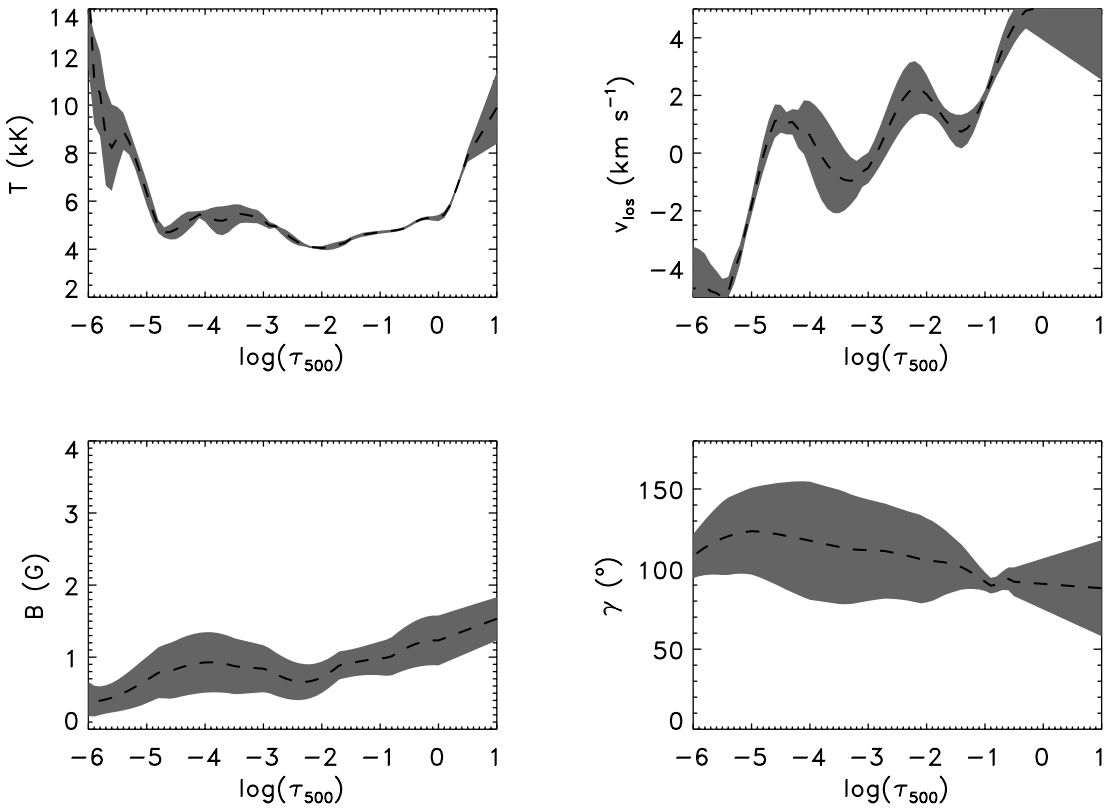

FIG. 8.—Point C: Average atmospheric stratification of temperature, line-of-sight velocity, magnetic field strength, and inclination away from the solar vertical. The shaded area represents the uncertainty.

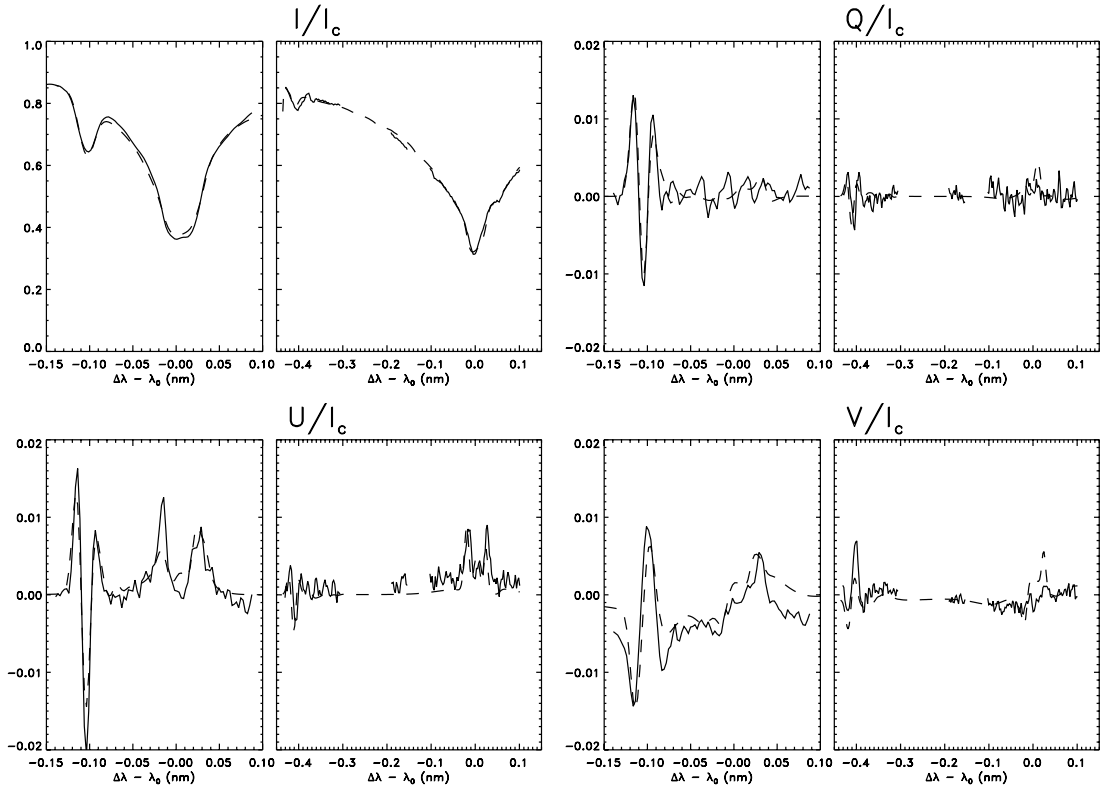

FIG. 9.—Point D: Observed (*solid line*) and synthetic (*dashed line*) Stokes profiles obtained from the fit, in units of the average quiet-Sun continuum intensity.

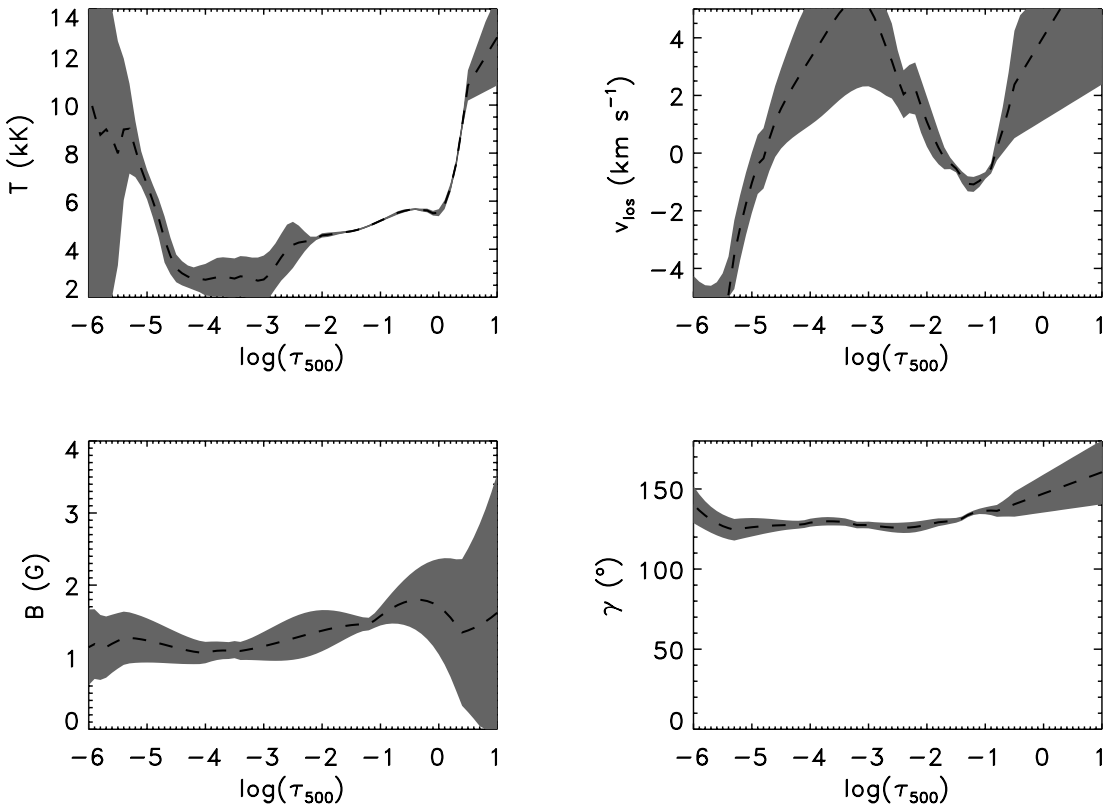

FIG. 10.—Point D: Average atmospheric stratification of temperature, line-of-sight velocity, magnetic field strength, and inclination away from the solar vertical. The shaded area represents the uncertainty.

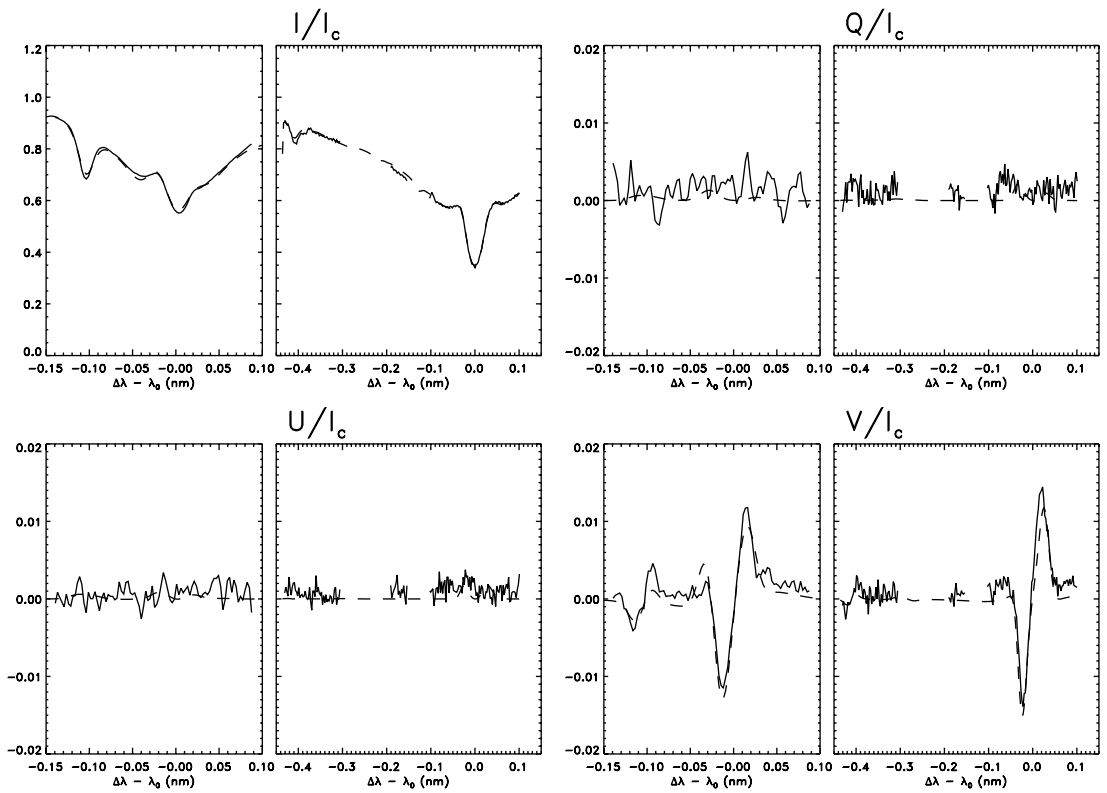

FIG. 11.—Point E: Observed (*solid line*) and synthetic (*dashed line*) Stokes profiles obtained from the fit, in units of the average quiet-Sun continuum intensity.

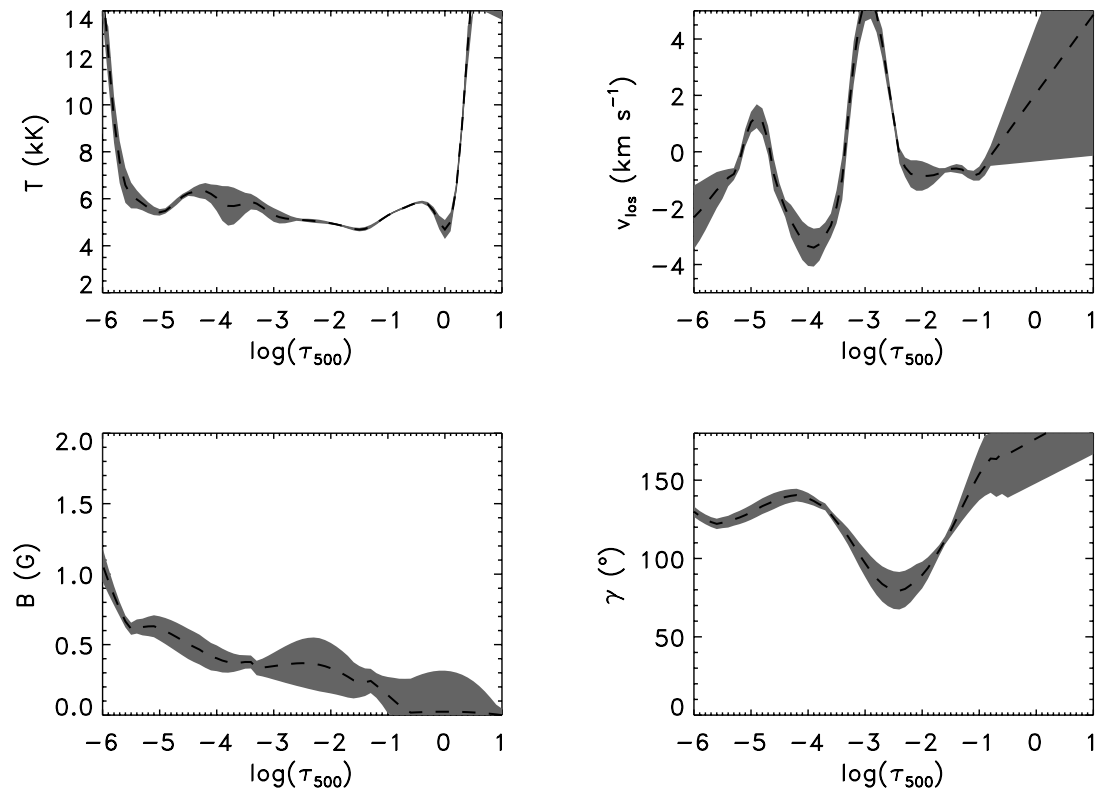

FIG. 12.—Point E: Average atmospheric stratification of temperature, line-of-sight velocity, magnetic field strength, and inclination away from the solar vertical. The shaded area represents the uncertainty.

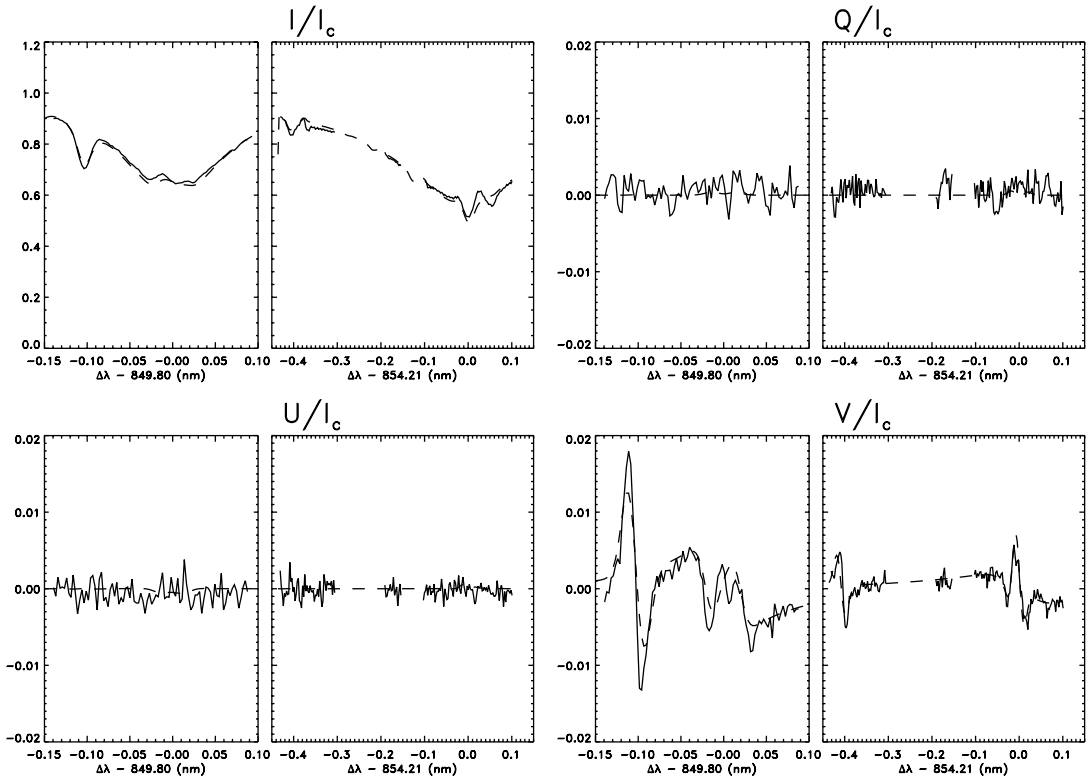

FIG. 13.—Point F: Observed (*solid line*) and synthetic (*dashed line*) Stokes profiles obtained from the fit, in units of the average quiet-Sun continuum intensity.

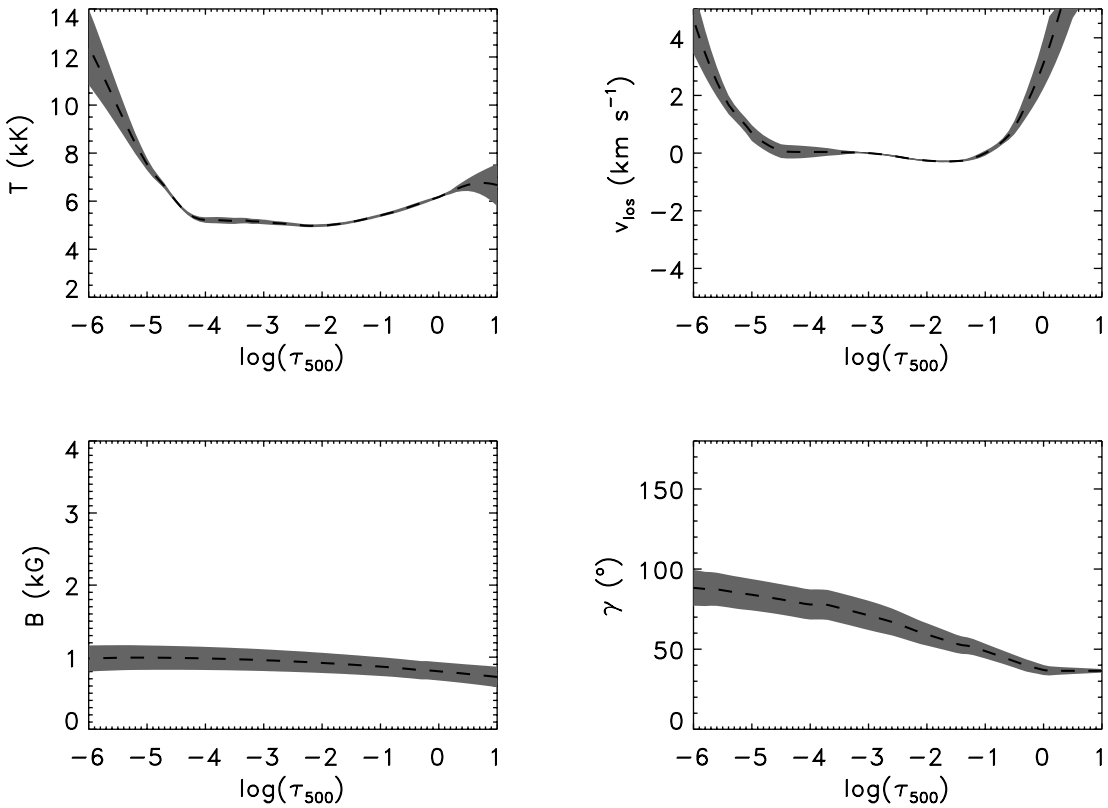

FIG. 14.—Point F: Average atmospheric stratification of temperature, line-of-sight velocity, magnetic field strength, and inclination away from the solar vertical. The shaded area represents the uncertainty.

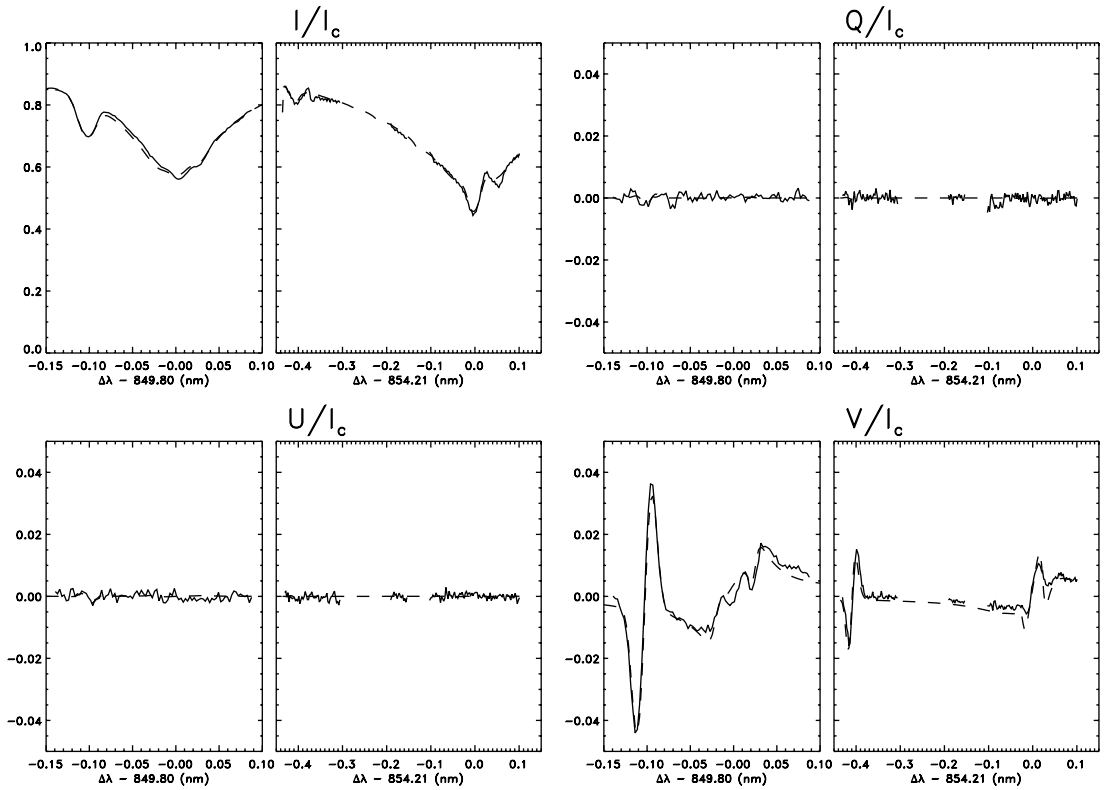

FIG. 15.—Point G: Observed (*solid line*) and synthetic (*dashed line*) Stokes profiles obtained from the fit, in units of the average quiet-Sun continuum intensity.

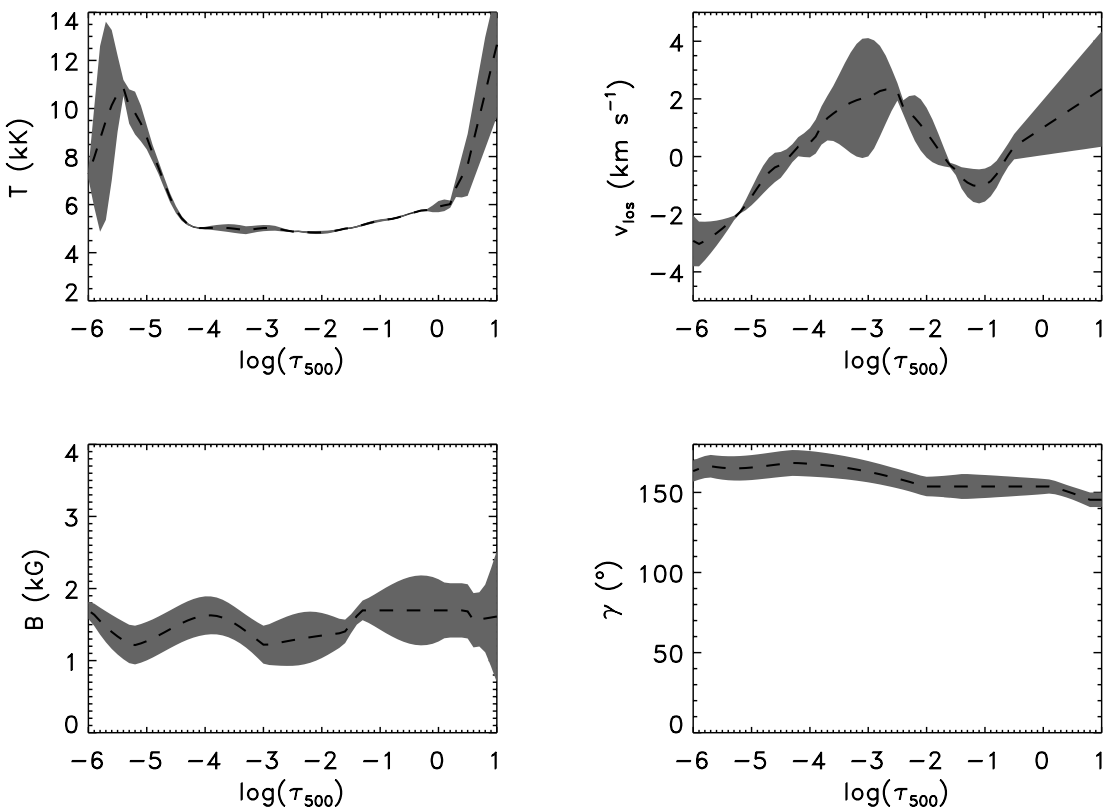

FIG. 16.—Point G: Average atmospheric stratification of temperature, line-of-sight velocity, magnetic field strength, and inclination away from the solar vertical. The shaded area represents the uncertainty.

TABLE 5

MODEL A: STRAY LIGHT FRACTION: 0.06

$\log(\tau_{500})$	Height (km)	Temp. (K)	Density (g cm^{-3})	Gas Press. (dyn cm^{-2})	Electron Press. (dyn cm^{-2})	$v_{\rm los}$ (cm s^{-1})	B (G)	γ (deg)
−5.90	1839.94	11321.40	3.024×10^{-14}	0.1836	9.165×10^{-2}	-3.631×10^{5}	1879.00	161.87
−5.80	1612.22	9315.70	1.886×10^{-13}	0.2148	0.1023	-2.830×10^{5}	1787.80	164.95
−5.70	1544.82	8432.90	2.460×10^{-13}	0.2527	0.1199	-1.580×10^{5}	1710.40	165.80
−5.60	1479.02	8030.60	3.096×10^{-13}	0.3004	0.1412	-4.673×10^{4}	1645.80	166.54
−5.50	1412.67	7864.80	3.834×10^{-13}	0.3607	0.1676	-1.434×10^{3}	1593.40	167.16
−5.40	1345.20	7680.00	4.868×10^{-13}	0.4380	0.1986	6.028×10^{4}	1628.80	167.67
−5.30	1272.91	7013.80	8.380×10^{-13}	0.5656	0.1892	9.692×10^{4}	1729.00	167.87
−5.20	1158.67	6245.80	2.737×10^{-12}	1.1943	9.956×10^{-2}	1.068×10^{5}	1835.60	167.41
−5.10	967.28	5480.40	2.565×10^{-11}	9.0463	4.479×10^{-2}	9.550×10^{4}	1946.50	167.16
−5.00	770.40	4711.10	1.579×10^{-10}	47.6494	1.118×10^{-2}	6.867×10^{4}	2060.10	167.15
−4.90	661.34	3968.50	4.491×10^{-10}	1.141×10^{2}	9.397×10^{-3}	3.190×10^{4}	2068.90	167.33
−4.80	618.32	3514.70	8.067×10^{-10}	1.816×10^{2}	6.695×10^{-3}	1.871×10^{4}	1983.60	167.67
−4.70	587.98	3163.80	1.318×10^{-9}	2.671×10^{2}	3.074×10^{-3}	-9.737×10^{3}	1897.70	168.09
−4.60	561.68	2875.50	2.007×10^{-9}	3.855×10^{2}	2.543×10^{-3}	-4.373×10^{4}	1912.60	168.75
−4.50	540.51	2886.90	2.673×10^{-9}	5.134×10^{2}	3.169×10^{-3}	-6.408×10^{4}	2001.50	168.83
−4.40	522.73	2835.80	3.403×10^{-9}	6.537×10^{2}	3.821×10^{-3}	-6.568×10^{4}	1972.60	168.78
−4.30	507.00	2781.60	4.214×10^{-9}	8.096×10^{2}	4.515×10^{-3}	-4.225×10^{4}	1926.70	168.68
−4.20	492.61	2899.50	5.124×10^{-9}	9.844×10^{2}	5.265×10^{-3}	-2.723×10^{4}	2001.60	168.59
−4.10	479.05	2821.20	6.076×10^{-9}	1.167×10^{3}	6.022×10^{-3}	-3.339×10^{4}	2086.00	168.49
−4.00	466.10	3042.40	7.114×10^{-9}	1.386×10^{3}	7.529×10^{-3}	-2.788×10^{4}	2100.20	168.48
−3.90	454.42	3301.70	7.676×10^{-9}	1.623×10^{3}	1.580×10^{-2}	5.037×10^{2}	2100.20	168.50
−3.80	444.05	3378.90	8.544×10^{-9}	1.849×10^{3}	2.136×10^{-2}	4.978×10^{3}	2100.20	168.56
−3.70	434.14	3465.50	9.410×10^{-9}	2.088×10^{3}	2.949×10^{-2}	1.607×10^{4}	2100.20	168.68
−3.60	424.66	3552.40	1.029×10^{-8}	2.340×10^{3}	4.040×10^{-2}	2.343×10^{4}	2100.20	168.66
−3.50	415.27	3588.00	1.129×10^{-8}	2.595×10^{3}	4.757×10^{-2}	2.808×10^{4}	2100.20	168.65
−3.40	405.56	3516.90	1.362×10^{-8}	3.068×10^{3}	4.374×10^{-2}	3.106×10^{4}	2100.20	168.64
−3.30	395.63	3561.80	1.501×10^{-8}	3.423×10^{3}	5.307×10^{-2}	4.259×10^{4}	2100.20	168.65
−3.20	385.42	3554.40	1.693×10^{-8}	3.853×10^{3}	5.621×10^{-2}	5.886×10^{4}	2100.20	168.66
−3.10	374.86	3577.10	1.893×10^{-8}	4.336×10^{3}	6.452×10^{-2}	7.433×10^{4}	2146.00	168.68
−3.00	364.05	3580.00	2.139×10^{-8}	4.904×10^{3}	7.046×10^{-2}	7.038×10^{4}	2212.10	168.43
−2.90	352.97	3588.80	2.418×10^{-8}	5.558×10^{3}	7.827×10^{-2}	6.984×10^{4}	2260.80	168.08
−2.80	341.81	3632.70	2.698×10^{-8}	6.277×10^{3}	9.505×10^{-2}	7.200×10^{4}	2215.30	167.70
−2.70	330.77	3681.70	2.998×10^{-8}	7.069×10^{3}	0.1165	8.073×10^{4}	2186.30	167.44
−2.60	319.81	3729.90	3.325×10^{-8}	7.941×10^{3}	0.1419	9.229×10^{4}	2146.70	167.83
−2.50	308.91	3783.50	3.672×10^{-8}	8.897×10^{3}	0.1745	1.016×10^{5}	2131.60	168.19
−2.40	297.99	3820.70	4.074×10^{-8}	9.968×10^{3}	0.2055	1.072×10^{5}	2133.70	168.48
−2.30	286.88	3838.30	4.559×10^{-8}	1.120×10^{4}	0.2312	1.078×10^{5}	2132.00	168.71
−2.20	275.42	3830.10	5.170×10^{-8}	1.268×10^{4}	0.2456	1.018×10^{5}	2126.30	168.82
−2.10	263.66	3851.50	5.816×10^{-8}	1.434×10^{4}	0.2799	8.830×10^{4}	2116.40	168.49
−2.00	251.77	3871.70	6.550×10^{-8}	1.624×10^{4}	0.3180	6.858×10^{4}	2102.80	168.33
−1.90	239.82	3906.30	7.339×10^{-8}	1.836×10^{4}	0.3731	4.435×10^{4}	2100.20	168.62
−1.80	227.84	3939.40	8.220×10^{-8}	2.074×10^{4}	0.4355	1.733×10^{4}	2098.10	168.82
−1.70	215.76	3957.30	9.259×10^{-8}	2.346×10^{4}	0.4912	-1.076×10^{4}	2051.40	168.84
−1.60	203.52	3976.10	1.044×10^{-7}	2.658×10^{4}	0.5553	-3.672×10^{4}	2021.70	168.80
−1.50	191.15	3995.90	1.177×10^{-7}	3.013×10^{4}	0.6293	-5.460×10^{4}	1997.40	168.82
−1.40	178.64	4015.90	1.329×10^{-7}	3.417×10^{4}	0.7126	-7.236×10^{4}	1972.40	168.82
−1.30	166.02	4035.00	1.501×10^{-7}	3.879×10^{4}	0.8064	-9.354×10^{4}	1947.40	168.82
−1.20	153.29	4054.20	1.697×10^{-7}	4.405×10^{4}	0.9127	-1.087×10^{5}	1922.80	168.82
−1.10	140.47	4075.20	1.917×10^{-7}	5.003×10^{4}	1.0368	-1.118×10^{5}	1899.20	168.81
−1.00	127.57	4100.80	2.163×10^{-7}	5.681×10^{4}	1.1884	-1.083×10^{5}	1877.00	168.82
−0.90	114.66	4134.80	2.432×10^{-7}	6.440×10^{4}	1.3839	-9.963×10^{4}	1838.00	168.81
−0.80	101.77	4180.40	2.720×10^{-7}	7.283×10^{4}	1.6457	-8.349×10^{4}	1779.60	168.72
−0.70	88.97	4240.70	3.021×10^{-7}	8.204×10^{4}	2.0052	-5.714×10^{4}	1729.50	168.79
−0.60	76.29	4320.60	3.323×10^{-7}	9.193×10^{4}	2.5160	-2.404×10^{4}	1689.20	168.69
−0.50	63.83	4420.10	3.659×10^{-7}	1.036×10^{5}	3.2550	1.324×10^{4}	1672.10	168.23
−0.40	51.61	4529.00	3.999×10^{-7}	1.160×10^{5}	4.2071	2.658×10^{4}	1665.30	168.50
−0.30	39.29	4638.30	4.291×10^{-7}	1.275×10^{5}	5.2945	3.991×10^{4}	1663.80	168.76
−0.20	26.66	4746.30	4.675×10^{-7}	1.421×10^{5}	6.6272	5.324×10^{4}	1667.90	169.03
−0.10	13.61	4844.10	5.031×10^{-7}	1.561×10^{5}	8.0122	6.658×10^{4}	1696.50	169.30
0.00	0.00	4963.60	5.482×10^{-7}	1.743×10^{5}	9.9544	7.991×10^{4}	1751.70	169.56

NOTE.—Table 5 is also available in machine-readable form in the electronic edition of the *Astrophysical Journal Supplement*.

TABLE 6

MODEL B: STRAY LIGHT FRACTION: 0.05

$\log(\tau_{500})$	Height (km)	Temp. (K)	Density (g cm^{-3})	Gas Press. (dyn cm^{-2})	Electron Press. (dyn cm^{-2})	$v_{\rm los}$ (cm s^{-1})	B (G)	γ (deg)
−5.90	2363.96	18591.50	2.529×10^{-14}	0.1936	9.678×10^{-2}	-4.233×10^{5}	1476.00	164.33
−5.80	2008.60	14524.20	3.688×10^{-14}	0.2215	0.1108	-4.067×10^{5}	1437.70	164.18
−5.70	1684.34	11886.40	4.697×10^{-14}	0.2568	0.1283	-3.668×10^{5}	1422.30	164.06
−5.60	1467.46	10303.90	2.397×10^{-13}	0.3032	0.1450	-3.158×10^{5}	1427.90	163.97
−5.50	1385.76	9027.80	3.293×10^{-13}	0.3630	0.1726	-2.599×10^{5}	1452.30	163.91
−5.40	1312.85	7635.60	4.953×10^{-13}	0.4406	0.1984	-2.057×10^{5}	1493.50	163.88
−5.30	1242.65	7271.90	7.002×10^{-13}	0.5412	0.2151	-1.581×10^{5}	1588.70	163.86
−5.20	1145.54	6484.40	1.860×10^{-12}	0.9045	0.1323	-1.118×10^{5}	1691.60	163.88
−5.10	964.64	5406.20	2.819×10^{-11}	9.7960	3.787×10^{-2}	-6.480×10^{4}	1763.20	163.91
−5.00	760.35	4489.30	1.900×10^{-10}	54.6213	7.325×10^{-3}	-5.492×10^{4}	1843.50	163.95
−4.90	659.49	3743.50	5.205×10^{-10}	1.248×10^{2}	7.899×10^{-3}	-3.094×10^{4}	1930.70	164.01
−4.80	622.23	3404.00	8.809×10^{-10}	1.920×10^{2}	5.184×10^{-3}	-1.081×10^{4}	2057.40	164.07
−4.70	593.50	3231.20	1.343×10^{-9}	2.779×10^{2}	3.897×10^{-3}	6.283×10^{3}	2118.10	164.15
−4.60	569.23	3118.70	1.925×10^{-9}	3.845×10^{2}	3.464×10^{-3}	1.986×10^{4}	2214.70	164.64
−4.50	548.83	3138.70	2.509×10^{-9}	5.043×10^{2}	4.444×10^{-3}	2.320×10^{4}	2310.70	165.16
−4.40	532.44	3353.60	2.925×10^{-9}	6.281×10^{2}	9.703×10^{-3}	4.375×10^{4}	2404.30	165.61
−4.30	518.60	3343.90	3.477×10^{-9}	7.445×10^{2}	1.054×10^{-2}	5.458×10^{4}	2493.50	165.97
−4.20	505.14	3365.60	4.057×10^{-9}	8.743×10^{2}	1.250×10^{-2}	4.884×10^{4}	2576.70	166.24
−4.10	491.86	3286.80	4.992×10^{-9}	1.051×10^{3}	1.124×10^{-2}	5.605×10^{4}	2651.90	166.54
−4.00	478.31	3150.50	6.310×10^{-9}	1.273×10^{3}	8.992×10^{-3}	6.844×10^{4}	2690.40	166.84
−3.90	464.76	2988.40	8.097×10^{-9}	1.555×10^{3}	7.564×10^{-3}	8.184×10^{4}	2731.90	167.05
−3.80	451.57	2823.40	9.545×10^{-9}	1.834×10^{3}	8.626×10^{-3}	9.648×10^{4}	2762.80	166.95
−3.70	438.75	2729.00	1.120×10^{-8}	2.151×10^{3}	9.804×10^{-3}	1.310×10^{5}	2776.10	166.75
−3.60	426.18	2668.80	1.309×10^{-8}	2.515×10^{3}	1.112×10^{-2}	1.814×10^{5}	2773.10	166.51
−3.50	413.81	2681.50	1.526×10^{-8}	2.932×10^{3}	1.258×10^{-2}	2.072×10^{5}	2755.60	166.24
−3.40	401.57	2610.10	1.776×10^{-8}	3.412×10^{3}	1.422×10^{-2}	2.281×10^{5}	2725.20	165.95
−3.30	389.42	2563.60	2.064×10^{-8}	3.965×10^{3}	1.607×10^{-2}	2.448×10^{5}	2683.80	165.59
−3.20	377.32	2534.20	2.397×10^{-8}	4.604×10^{3}	1.814×10^{-2}	2.554×10^{5}	2633.20	164.45
−3.10	365.24	2574.10	2.781×10^{-8}	5.343×10^{3}	2.048×10^{-2}	2.579×10^{5}	2575.00	164.38
−3.00	353.16	2655.40	3.228×10^{-8}	6.201×10^{3}	2.312×10^{-2}	2.507×10^{5}	2511.10	164.31
−2.90	341.05	2683.40	3.747×10^{-8}	7.198×10^{3}	2.611×10^{-2}	2.219×10^{5}	2443.30	163.87
−2.80	328.90	2867.20	4.351×10^{-8}	8.359×10^{3}	2.950×10^{-2}	1.835×10^{5}	2373.30	163.24
−2.70	317.49	3148.60	4.791×10^{-8}	9.660×10^{3}	4.324×10^{-2}	1.435×10^{5}	2302.80	162.64
−2.60	307.62	3365.10	5.061×10^{-8}	1.090×10^{4}	7.232×10^{-2}	1.186×10^{5}	2233.70	162.07
−2.50	298.93	3578.00	5.291×10^{-8}	1.212×10^{4}	0.1279	9.518×10^{4}	2167.70	161.57
−2.40	291.22	3775.50	5.485×10^{-8}	1.326×10^{4}	0.2215	5.797×10^{4}	2110.10	161.16
−2.30	284.14	3947.40	5.663×10^{-8}	1.431×10^{4}	0.3485	2.489×10^{4}	2103.20	160.88
−2.20	277.21	4083.50	5.871×10^{-8}	1.535×10^{4}	0.4859	-1.431×10^{3}	2097.30	160.73
−2.10	270.04	4201.20	6.114×10^{-8}	1.645×10^{4}	0.6348	-1.908×10^{4}	2059.70	160.75
−2.00	262.11	4247.60	6.235×10^{-8}	1.696×10^{4}	0.7020	-2.907×10^{4}	2022.00	160.89
−1.90	253.12	4274.60	6.705×10^{-8}	1.835×10^{4}	0.7761	-3.315×10^{4}	1995.60	161.17
−1.80	243.36	4283.60	7.313×10^{-8}	2.006×10^{4}	0.8386	-3.307×10^{4}	1979.20	161.52
−1.70	232.88	4277.20	8.082×10^{-8}	2.214×10^{4}	0.8892	-3.056×10^{4}	1971.50	161.93
−1.60	221.72	4263.40	9.020×10^{-8}	2.462×10^{4}	0.9354	-2.738×10^{4}	1971.20	162.37
−1.50	209.96	4251.50	1.012×10^{-7}	2.756×10^{4}	0.9900	-2.526×10^{4}	1976.90	162.83
−1.40	197.69	4249.60	1.138×10^{-7}	3.097×10^{4}	1.0683	-2.595×10^{4}	1987.30	163.25
−1.30	185.02	4263.90	1.277×10^{-7}	3.486×10^{4}	1.1876	-3.054×10^{4}	2001.10	163.64
−1.20	172.06	4292.00	1.428×10^{-7}	3.925×10^{4}	1.3532	-3.751×10^{4}	2016.90	164.03
−1.10	158.90	4337.10	1.589×10^{-7}	4.412×10^{4}	1.5853	-4.466×10^{4}	2016.30	164.19
−1.00	145.58	4395.50	1.759×10^{-7}	4.950×10^{4}	1.8915	-4.982×10^{4}	2024.60	164.33
−0.90	132.08	4466.20	1.937×10^{-7}	5.539×10^{4}	2.2872	-4.927×10^{4}	2042.30	164.32
−0.80	118.37	4538.90	2.130×10^{-7}	6.190×10^{4}	2.7555	-4.401×10^{4}	2036.80	164.21
−0.70	104.49	4621.90	2.365×10^{-7}	7.001×10^{4}	3.3756	-3.290×10^{4}	2025.40	163.91
−0.60	90.56	4723.00	2.609×10^{-7}	7.891×10^{4}	4.1883	-2.179×10^{4}	2011.80	163.39
−0.50	76.44	4831.60	2.868×10^{-7}	8.875×10^{4}	5.1807	-1.068×10^{4}	1995.80	162.64
−0.40	62.01	4922.10	3.168×10^{-7}	9.985×10^{4}	6.2351	4.334×10^{2}	1977.30	161.61
−0.30	47.24	4997.20	3.514×10^{-7}	1.125×10^{5}	7.3653	1.154×10^{4}	1956.00	159.30
−0.20	32.00	5050.50	3.873×10^{-7}	1.253×10^{5}	8.4316	2.266×10^{4}	1943.00	156.07
−0.10	16.18	5089.80	4.303×10^{-7}	1.403×10^{5}	9.5587	3.377×10^{4}	1904.10	155.40
0.00	0.00	5170.40	4.804×10^{-7}	1.591×10^{5}	11.3675	4.488×10^{4}	1873.10	154.73

NOTE.—Table 6 is also available in machine-readable form in the electronic edition of the *Astrophysical Journal Supplement*.

TABLE 7

MODEL C: STRAY LIGHT FRACTION: 0.23

$\log(\tau_{500})$	Height (km)	Temp. (K)	Density (g cm^{-3})	Gas Press. (dyn cm^{-2})	Electron Press. (dyn cm^{-2})	$v_{\rm los}$ (cm s^{-1})	B (G)	γ (deg)
−5.90	2204.78	11070.80	2.586×10^{-14}	0.1839	9.174×10^{-2}	-4.640×10^{5}	390.68	110.91
−5.80	1940.04	10461.80	1.666×10^{-13}	0.2149	0.1032	-4.625×10^{5}	396.80	113.43
−5.70	1867.07	8667.10	2.390×10^{-13}	0.2527	0.1201	-4.788×10^{5}	413.79	115.62
−5.60	1799.42	8227.80	3.006×10^{-13}	0.3003	0.1419	-4.856×10^{5}	436.89	117.52
−5.50	1729.33	8645.90	3.425×10^{-13}	0.3609	0.1713	-4.997×10^{5}	466.54	119.14
−5.40	1653.74	8908.20	4.016×10^{-13}	0.4365	0.2074	-4.837×10^{5}	501.86	120.50
−5.30	1576.67	8466.20	5.161×10^{-13}	0.5307	0.2508	-4.101×10^{5}	541.99	121.61
−5.20	1503.01	7816.60	7.078×10^{-13}	0.6484	0.2941	-3.533×10^{5}	586.06	122.50
−5.10	1426.94	7080.90	1.271×10^{-12}	0.8492	0.2729	-2.652×10^{5}	633.19	123.19
−5.00	1309.30	6331.20	4.115×10^{-12}	1.8166	0.1484	-1.821×10^{5}	682.52	123.69
−4.90	1119.00	5597.50	3.242×10^{-11}	11.6906	7.027×10^{-2}	-9.330×10^{4}	733.19	123.48
−4.80	925.42	4944.80	1.752×10^{-10}	55.5025	2.407×10^{-2}	-1.101×10^{4}	784.31	123.09
−4.70	807.03	4694.10	4.597×10^{-10}	1.382×10^{2}	2.191×10^{-2}	5.899×10^{4}	800.38	122.60
−4.60	746.88	4714.40	7.643×10^{-10}	2.308×10^{2}	3.319×10^{-2}	1.110×10^{5}	810.69	122.05
−4.50	709.68	4822.60	1.035×10^{-9}	3.195×10^{2}	5.211×10^{-2}	1.192×10^{5}	833.77	121.43
−4.40	683.07	4991.10	1.263×10^{-9}	4.037×10^{2}	8.940×10^{-2}	1.036×10^{5}	861.71	120.65
−4.30	663.26	5166.10	1.446×10^{-9}	4.786×10^{2}	0.1542	1.084×10^{5}	885.43	120.04
−4.20	647.49	5288.00	1.609×10^{-9}	5.452×10^{2}	0.2285	8.392×10^{4}	904.48	119.28
−4.10	634.16	5442.70	1.741×10^{-9}	6.072×10^{2}	0.3635	8.969×10^{4}	918.43	118.50
−4.00	621.18	5383.30	1.955×10^{-9}	6.742×10^{2}	0.3300	6.030×10^{4}	926.81	117.72
−3.90	605.64	5283.10	2.277×10^{-9}	7.705×10^{2}	0.2750	2.376×10^{4}	929.21	116.92
−3.80	587.49	5200.60	2.700×10^{-9}	8.995×10^{2}	0.2452	-1.112×10^{4}	925.15	116.13
−3.70	568.04	5181.50	3.172×10^{-9}	1.053×10^{3}	0.2580	-4.121×10^{4}	914.45	115.36
−3.60	549.46	5262.80	3.637×10^{-9}	1.226×10^{3}	0.3440	-6.538×10^{4}	897.77	114.60
−3.50	533.33	5394.70	4.044×10^{-9}	1.398×10^{3}	0.5129	-8.302×10^{4}	876.03	113.86
−3.40	519.06	5468.70	4.465×10^{-9}	1.564×10^{3}	0.6564	-9.350×10^{4}	865.32	113.14
−3.30	504.60	5434.60	5.057×10^{-9}	1.761×10^{3}	0.6459	-9.620×10^{4}	859.72	112.44
−3.20	488.69	5387.30	5.854×10^{-9}	2.020×10^{3}	0.6245	-9.048×10^{4}	853.41	112.13
−3.10	471.50	5354.30	6.752×10^{-9}	2.316×10^{3}	0.6271	-6.430×10^{4}	846.72	111.94
−3.00	452.30	5199.20	8.185×10^{-9}	2.726×10^{3}	0.4955	-5.135×10^{4}	839.99	111.77
−2.90	432.41	4993.50	1.143×10^{-8}	3.655×10^{3}	0.4352	-1.734×10^{4}	812.46	111.61
−2.80	414.01	4961.00	1.327×10^{-8}	4.217×10^{3}	0.4700	2.356×10^{4}	769.75	111.44
−2.70	396.57	4766.10	1.626×10^{-8}	4.962×10^{3}	0.4557	6.797×10^{4}	731.64	111.18
−2.60	380.79	4603.50	1.943×10^{-8}	5.729×10^{3}	0.4591	1.125×10^{5}	699.72	110.46
−2.50	366.39	4428.90	2.336×10^{-8}	6.624×10^{3}	0.4424	1.538×10^{5}	675.55	109.70
−2.40	352.84	4278.70	2.797×10^{-8}	7.665×10^{3}	0.4130	1.885×10^{5}	660.70	108.90
−2.30	339.49	4177.90	3.303×10^{-8}	8.836×10^{3}	0.3935	2.132×10^{5}	656.75	108.05
−2.20	325.95	4092.10	3.901×10^{-8}	1.022×10^{4}	0.3748	2.245×10^{5}	665.27	107.15
−2.10	312.20	4071.40	4.506×10^{-8}	1.175×10^{4}	0.3960	2.204×10^{5}	687.32	106.19
−2.00	298.30	4049.50	5.221×10^{-8}	1.354×10^{4}	0.4171	2.036×10^{5}	721.91	105.48
−1.90	284.41	4077.20	5.936×10^{-8}	1.550×10^{4}	0.4829	1.785×10^{5}	767.54	105.09
−1.80	270.70	4130.00	6.666×10^{-8}	1.763×10^{4}	0.5840	1.492×10^{5}	822.73	104.69
−1.70	257.17	4198.30	7.410×10^{-8}	1.992×10^{4}	0.7207	1.200×10^{5}	885.62	104.27
−1.60	243.84	4275.70	8.279×10^{-8}	2.267×10^{4}	0.9018	9.500×10^{4}	901.52	103.39
−1.50	230.81	4435.40	8.995×10^{-8}	2.555×10^{4}	1.2557	7.843×10^{4}	917.60	102.29
−1.40	217.82	4525.80	9.900×10^{-8}	2.869×10^{4}	1.5434	7.448×10^{4}	933.38	101.21
−1.30	204.58	4601.50	1.094×10^{-7}	3.223×10^{4}	1.8482	8.626×10^{4}	948.40	99.31
−1.20	190.92	4641.30	1.207×10^{-7}	3.588×10^{4}	2.1004	1.123×10^{5}	962.19	97.04
−1.10	176.72	4677.30	1.339×10^{-7}	4.010×10^{4}	2.3820	1.500×10^{5}	974.27	94.66
−1.00	162.06	4710.20	1.491×10^{-7}	4.497×10^{4}	2.6976	1.968×10^{5}	984.17	92.18
−0.90	147.01	4733.70	1.670×10^{-7}	5.062×10^{4}	3.0317	2.503×10^{5}	991.44	89.60
−0.80	131.64	4760.20	1.872×10^{-7}	5.708×10^{4}	3.4216	3.077×10^{5}	1012.90	90.45
−0.70	115.98	4796.20	2.096×10^{-7}	6.437×10^{4}	3.9009	3.583×10^{5}	1063.00	92.75
−0.60	100.15	4861.00	2.359×10^{-7}	7.345×10^{4}	4.6203	4.040×10^{5}	1108.10	93.90
−0.50	84.23	4985.30	2.612×10^{-7}	8.339×10^{4}	5.7571	4.419×10^{5}	1147.60	92.07
−0.40	68.01	5131.80	2.874×10^{-7}	9.445×10^{4}	7.2503	4.713×10^{5}	1180.60	91.81
−0.30	51.49	5242.70	3.188×10^{-7}	1.070×10^{5}	8.8398	4.939×10^{5}	1206.40	91.54
−0.20	34.61	5294.70	3.535×10^{-7}	1.199×10^{5}	10.1446	4.985×10^{5}	1224.10	91.27
−0.10	17.39	5281.90	4.010×10^{-7}	1.357×10^{5}	11.0721	5.031×10^{5}	1233.00	91.01
0.00	0.00	5293.70	4.521×10^{-7}	1.532×10^{5}	12.3345	5.078×10^{5}	1232.30	90.74

NOTE.—Table 7 is also available in machine-readable form in the electronic edition of the *Astrophysical Journal Supplement*.

TABLE 8

MODEL D: STRAY LIGHT FRACTION: 0.27

$\log(\tau_{500})$	Height (km)	Temp. (K)	Density (g cm^{-3})	Gas Press. (dyn cm^{-2})	Electron Press. (dyn cm^{-2})	$v_{\rm los}$ (cm s^{-1})	B (G)	γ (deg)
−5.90	1928.65	9603.70	1.716×10^{-13}	0.2016	9.606×10^{-2}	-7.435×10^{5}	1181.60	136.60
−5.80	1868.74	8761.10	2.166×10^{-13}	0.2317	0.1102	-7.288×10^{5}	1134.80	133.47
−5.70	1806.29	8987.60	2.455×10^{-13}	0.2695	0.1282	-6.922×10^{5}	1140.20	130.82
−5.60	1739.75	8620.40	3.016×10^{-13}	0.3169	0.1505	-6.383×10^{5}	1186.40	128.64
−5.50	1673.60	7990.80	3.918×10^{-13}	0.3766	0.1761	-5.716×10^{5}	1227.10	126.88
−5.40	1603.66	8985.30	4.127×10^{-13}	0.4526	0.2151	-4.894×10^{5}	1262.70	125.53
−5.30	1526.27	9016.10	4.971×10^{-13}	0.5469	0.2599	-3.524×10^{5}	1267.50	124.55
−5.20	1450.31	8169.00	6.748×10^{-13}	0.6623	0.3093	-2.585×10^{5}	1259.80	125.16
−5.10	1376.99	7348.80	1.068×10^{-12}	0.8209	0.3185	-1.758×10^{5}	1247.80	125.68
−5.00	1284.49	6687.90	2.448×10^{-12}	1.2735	0.2250	-1.031×10^{5}	1232.40	126.12
−4.90	1128.93	5998.70	1.185×10^{-11}	4.6707	0.1197	-3.917×10^{4}	1214.30	126.49
−4.80	926.49	5299.50	8.360×10^{-11}	28.4193	4.826×10^{-2}	-1.841×10^{4}	1194.30	126.80
−4.70	765.28	4405.70	3.767×10^{-10}	1.063×10^{2}	1.140×10^{-2}	4.955×10^{4}	1173.10	127.04
−4.60	684.54	3723.70	8.984×10^{-10}	2.142×10^{2}	1.167×10^{-2}	1.097×10^{5}	1151.60	127.24
−4.50	649.56	3202.30	1.609×10^{-9}	3.299×10^{2}	3.994×10^{-3}	1.545×10^{5}	1130.50	127.38
−4.40	620.02	2999.40	2.560×10^{-9}	4.919×10^{2}	3.065×10^{-3}	1.930×10^{5}	1110.50	127.48
−4.30	597.08	2861.80	3.488×10^{-9}	6.700×10^{2}	3.895×10^{-3}	2.289×10^{5}	1092.60	127.55
−4.20	578.47	2773.80	4.487×10^{-9}	8.620×10^{2}	4.743×10^{-3}	2.629×10^{5}	1077.30	127.72
−4.10	562.31	2767.10	5.587×10^{-9}	1.073×10^{3}	5.636×10^{-3}	2.956×10^{5}	1065.60	128.11
−4.00	547.69	2729.10	6.813×10^{-9}	1.309×10^{3}	6.594×10^{-3}	3.276×10^{5}	1064.10	128.97
−3.90	533.98	2782.20	8.087×10^{-9}	1.554×10^{3}	7.557×10^{-3}	3.595×10^{5}	1079.10	129.42
−3.80	520.78	2831.00	9.537×10^{-9}	1.832×10^{3}	8.620×10^{-3}	3.918×10^{5}	1089.00	129.73
−3.70	507.93	2849.40	1.119×10^{-8}	2.150×10^{3}	9.799×10^{-3}	4.247×10^{5}	1093.00	129.85
−3.60	495.36	2820.10	1.308×10^{-8}	2.514×10^{3}	1.111×10^{-2}	4.566×10^{5}	1091.70	129.80
−3.50	482.98	2777.70	1.526×10^{-8}	2.931×10^{3}	1.258×10^{-2}	4.853×10^{5}	1104.60	129.62
−3.40	470.73	2871.40	1.776×10^{-8}	3.411×10^{3}	1.422×10^{-2}	5.089×10^{5}	1086.30	129.32
−3.30	458.57	2847.30	2.063×10^{-8}	3.964×10^{3}	1.606×10^{-2}	5.252×10^{5}	1100.20	128.48
−3.20	446.47	2757.70	2.396×10^{-8}	4.603×10^{3}	1.814×10^{-2}	5.322×10^{5}	1115.90	127.51
−3.10	434.39	2691.60	2.781×10^{-8}	5.342×10^{3}	2.048×10^{-2}	5.278×10^{5}	1133.30	127.52
−3.00	422.30	2738.80	3.227×10^{-8}	6.200×10^{3}	2.312×10^{-2}	5.082×10^{5}	1152.10	127.52
−2.90	410.19	2960.20	3.746×10^{-8}	7.197×10^{3}	2.611×10^{-2}	4.699×10^{5}	1172.10	127.04
−2.80	399.22	3298.80	3.924×10^{-8}	8.289×10^{3}	5.115×10^{-2}	4.222×10^{5}	1193.00	126.60
−2.70	390.75	3668.40	3.951×10^{-8}	9.280×10^{3}	0.1344	3.679×10^{5}	1214.70	126.24
−2.60	384.07	3983.00	3.916×10^{-8}	9.988×10^{3}	0.2971	3.193×10^{5}	1236.90	125.96
−2.50	377.93	4178.70	3.948×10^{-8}	1.057×10^{4}	0.4476	2.576×10^{5}	1259.40	125.81
−2.40	371.02	4276.60	3.825×10^{-8}	1.048×10^{4}	0.5195	2.040×10^{5}	1281.90	125.80
−2.30	362.63	4319.60	3.913×10^{-8}	1.082×10^{4}	0.5661	2.222×10^{5}	1304.30	125.96
−2.20	353.09	4350.90	4.206×10^{-8}	1.172×10^{4}	0.6272	2.241×10^{5}	1326.20	126.33
−2.10	342.13	4451.20	4.194×10^{-8}	1.195×10^{4}	0.7227	1.631×10^{5}	1347.50	126.90
−2.00	328.79	4575.40	4.184×10^{-8}	1.226×10^{4}	0.8422	1.088×10^{5}	1367.90	127.65
−1.90	313.81	4603.30	4.678×10^{-8}	1.379×10^{4}	0.9515	6.074×10^{4}	1387.00	128.50
−1.80	298.45	4638.80	5.227×10^{-8}	1.553×10^{4}	1.0834	1.847×10^{4}	1404.50	129.23
−1.70	282.90	4680.10	5.921×10^{-8}	1.774×10^{4}	1.2548	-1.836×10^{4}	1420.20	129.58
−1.60	267.22	4713.00	6.625×10^{-8}	2.000×10^{4}	1.4250	-3.552×10^{4}	1433.70	129.98
−1.50	251.39	4747.50	7.523×10^{-8}	2.287×10^{4}	1.6399	-5.362×10^{4}	1444.70	130.46
−1.40	235.57	4801.90	8.485×10^{-8}	2.609×10^{4}	1.9162	-8.390×10^{4}	1452.80	131.53
−1.30	219.65	4877.20	9.511×10^{-8}	2.971×10^{4}	2.2733	-1.065×10^{5}	1457.90	133.64
−1.20	203.50	4969.20	1.061×10^{-7}	3.378×10^{4}	2.7275	-1.085×10^{5}	1459.50	135.15
−1.10	187.07	5073.50	1.181×10^{-7}	3.837×10^{4}	3.3034	-9.642×10^{4}	1509.00	136.04
−1.00	170.38	5186.40	1.311×10^{-7}	4.356×10^{4}	4.0444	-7.776×10^{4}	1571.80	136.41
−0.90	153.58	5292.50	1.458×10^{-7}	4.941×10^{4}	4.9611	-5.271×10^{4}	1629.40	136.53
−0.80	136.85	5402.90	1.617×10^{-7}	5.594×10^{4}	6.1759	1.811×10^{4}	1680.70	136.34
−0.70	120.42	5515.40	1.787×10^{-7}	6.313×10^{4}	7.8017	8.013×10^{4}	1724.20	137.55
−0.60	104.17	5589.50	1.962×10^{-7}	7.023×10^{4}	9.3529	1.530×10^{5}	1758.70	138.95
−0.50	87.80	5640.70	2.170×10^{-7}	7.839×10^{4}	10.9050	2.380×10^{5}	1782.70	140.49
−0.40	71.18	5668.50	2.419×10^{-7}	8.781×10^{4}	12.3162	2.714×10^{5}	1795.10	141.82
−0.30	54.07	5632.50	2.758×10^{-7}	9.948×10^{4}	12.7810	3.047×10^{5}	1794.50	143.16
−0.20	36.39	5612.40	3.139×10^{-7}	1.128×10^{5}	13.6348	3.380×10^{5}	1779.50	144.49
−0.10	18.31	5497.80	3.703×10^{-7}	1.304×10^{5}	13.2526	3.714×10^{5}	1748.80	145.82
0.00	0.00	5519.70	4.176×10^{-7}	1.476×10^{5}	14.9401	4.047×10^{5}	1701.20	147.16

NOTE.—Table 8 is also available in machine-readable form in the electronic edition of the *Astrophysical Journal Supplement*.

TABLE 9

MODEL E: STRAY LIGHT FRACTION: 0.43

$\log(\tau_{500})$	Height (km)	Temp. (K)	Density (g cm^{-3})	Gas Press. (dyn cm^{-2})	Electron Press. (dyn cm^{-2})	$v_{\rm los}$ (cm s^{-1})	B (G)	γ (deg)
−5.90	2091.52	12159.70	3.495×10^{-14}	0.1837	9.179×10^{-2}	-2.112×10^{5}	952.67	127.19
−5.80	1890.08	9370.60	1.875×10^{-13}	0.2148	0.1023	-1.871×10^{5}	847.98	125.02
−5.70	1825.30	7567.00	2.846×10^{-13}	0.2540	0.1161	-1.614×10^{5}	752.09	123.28
−5.60	1752.98	6572.40	6.207×10^{-13}	0.3438	8.254×10^{-2}	-1.360×10^{5}	664.73	122.10
−5.50	1642.22	6139.00	1.633×10^{-12}	0.7016	5.980×10^{-2}	-1.166×10^{5}	612.75	122.88
−5.40	1504.72	5971.40	4.499×10^{-12}	1.7885	6.825×10^{-2}	-9.204×10^{4}	628.48	123.52
−5.30	1372.30	5799.90	1.225×10^{-11}	4.6230	7.380×10^{-2}	-7.916×10^{4}	625.00	124.94
−5.20	1251.38	5619.00	3.100×10^{-11}	11.2287	7.290×10^{-2}	-3.163×10^{4}	629.46	126.19
−5.10	1150.47	5481.70	6.702×10^{-11}	23.6002	7.349×10^{-2}	5.021×10^{4}	630.43	127.70
−5.00	1074.15	5420.40	1.198×10^{-10}	41.6593	8.306×10^{-2}	1.050×10^{5}	614.95	129.46
−4.90	1020.05	5482.80	1.775×10^{-10}	62.4239	0.1217	1.263×10^{5}	596.51	131.45
−4.80	984.21	5666.30	2.237×10^{-10}	81.3820	0.2275	1.065×10^{5}	575.69	133.43
−4.70	960.85	5878.10	2.554×10^{-10}	96.5521	0.4228	3.929×10^{4}	553.11	135.03
−4.60	944.52	6090.50	2.761×10^{-10}	1.084×10^{2}	0.7401	-8.048×10^{4}	529.38	136.65
−4.50	931.71	6227.50	2.943×10^{-10}	1.184×10^{2}	1.0513	-1.478×10^{5}	505.15	138.09
−4.40	919.83	6296.40	3.151×10^{-10}	1.283×10^{2}	1.2714	-2.008×10^{5}	484.65	139.26
−4.30	907.46	6317.40	3.412×10^{-10}	1.394×10^{2}	1.3872	-2.451×10^{5}	464.69	140.04
−4.20	893.95	6326.70	3.744×10^{-10}	1.532×10^{2}	1.4844	-2.808×10^{5}	438.05	140.49
−4.10	877.57	6207.50	4.278×10^{-10}	1.712×10^{2}	1.2143	-3.153×10^{5}	414.55	139.67
−4.00	855.19	6033.40	5.164×10^{-10}	2.004×10^{2}	0.8877	-3.346×10^{5}	403.40	138.41
−3.90	824.16	5799.20	6.758×10^{-10}	2.515×10^{2}	0.5690	-3.400×10^{5}	387.11	136.72
−3.80	787.03	5694.80	9.056×10^{-10}	3.308×10^{2}	0.5047	-3.280×10^{5}	376.15	134.55
−3.70	751.54	5689.10	1.178×10^{-9}	4.297×10^{2}	0.5701	-2.966×10^{5}	371.20	132.97
−3.60	721.12	5738.60	1.461×10^{-9}	5.375×10^{2}	0.7253	-2.614×10^{5}	371.80	128.15
−3.50	695.48	5807.60	1.740×10^{-9}	6.482×10^{2}	0.9476	-1.953×10^{5}	377.07	123.56
−3.40	673.26	5876.10	2.020×10^{-9}	7.614×10^{2}	1.2156	-9.351×10^{4}	376.64	119.05
−3.30	651.25	5795.30	2.408×10^{-9}	8.947×10^{2}	1.0879	1.203×10^{5}	334.40	114.05
−3.20	625.36	5639.50	3.006×10^{-9}	1.086×10^{3}	0.8215	3.158×10^{5}	337.44	108.33
−3.10	594.36	5460.90	3.946×10^{-9}	1.380×10^{3}	0.6000	4.574×10^{5}	342.32	102.45
−3.00	560.04	5309.80	5.331×10^{-9}	1.813×10^{3}	0.4874	5.426×10^{5}	347.91	97.03
−2.90	526.30	5217.60	7.135×10^{-9}	2.384×10^{3}	0.4710	5.473×10^{5}	353.61	91.78
−2.80	495.67	5162.70	9.208×10^{-9}	3.045×10^{3}	0.4976	4.886×10^{5}	359.06	87.29
−2.70	468.23	5132.10	1.149×10^{-8}	3.775×10^{3}	0.5489	3.843×10^{5}	363.67	83.73
−2.60	443.35	5123.90	1.392×10^{-8}	4.567×10^{3}	0.6233	2.490×10^{5}	366.97	81.39
−2.50	420.34	5094.70	1.672×10^{-8}	5.456×10^{3}	0.6833	1.193×10^{5}	368.56	79.82
−2.40	398.63	5077.60	1.978×10^{-8}	6.431×10^{3}	0.7599	-1.296×10^{4}	367.77	79.43
−2.30	377.95	5055.90	2.322×10^{-8}	7.519×10^{3}	0.8394	-5.472×10^{4}	364.22	80.58
−2.20	358.09	5030.00	2.712×10^{-8}	8.735×10^{3}	0.9232	-7.812×10^{4}	357.32	83.11
−2.10	338.93	4997.30	3.155×10^{-8}	1.010×10^{4}	1.0100	-8.425×10^{4}	346.81	86.53
−2.00	320.42	4956.50	3.664×10^{-8}	1.163×10^{4}	1.0991	-8.590×10^{4}	332.84	89.43
−1.90	302.54	4908.60	4.247×10^{-8}	1.335×10^{4}	1.1904	-8.551×10^{4}	315.50	93.90
−1.80	285.29	4850.10	4.926×10^{-8}	1.530×10^{4}	1.2782	-8.296×10^{4}	295.23	99.44
−1.70	268.68	4779.20	5.728×10^{-8}	1.753×10^{4}	1.3545	-7.660×10^{4}	272.32	105.24
−1.60	252.63	4715.50	6.641×10^{-8}	2.005×10^{4}	1.4316	-6.614×10^{4}	246.83	111.50
−1.50	236.88	4686.70	7.605×10^{-8}	2.282×10^{4}	1.5466	-6.073×10^{4}	236.52	117.84
−1.40	221.08	4717.80	8.531×10^{-8}	2.577×10^{4}	1.7565	-5.939×10^{4}	233.16	125.10
−1.30	205.06	4815.00	9.539×10^{-8}	2.941×10^{4}	2.1371	-6.302×10^{4}	242.74	132.63
−1.20	188.74	4964.50	1.052×10^{-7}	3.344×10^{4}	2.6944	-7.887×10^{4}	209.99	139.96
−1.10	171.95	5134.70	1.155×10^{-7}	3.798×10^{4}	3.4502	-8.496×10^{4}	176.21	147.11
−1.00	154.90	5293.20	1.272×10^{-7}	4.312×10^{4}	4.4516	-7.742×10^{4}	141.59	153.89
−0.90	138.05	5423.50	1.407×10^{-7}	4.886×10^{4}	5.7070	-5.213×10^{4}	106.38	159.31
−0.80	121.66	5533.00	1.556×10^{-7}	5.514×10^{4}	7.2382	-1.414×10^{4}	70.91	163.80
−0.70	105.66	5629.90	1.699×10^{-7}	6.126×10^{4}	9.0203	1.364×10^{4}	43.78	163.51
−0.60	90.09	5735.10	1.872×10^{-7}	6.874×10^{4}	11.5747	4.142×10^{4}	17.90	167.23
−0.50	75.16	5826.60	2.055×10^{-7}	7.670×10^{4}	14.5523	6.920×10^{4}	19.66	166.60
−0.40	60.30	5859.00	2.264×10^{-7}	8.496×10^{4}	16.4494	9.697×10^{4}	21.19	168.60
−0.30	44.69	5771.70	2.659×10^{-7}	9.829×10^{4}	15.6271	1.248×10^{5}	22.44	170.60
−0.20	29.24	5488.40	3.720×10^{-7}	1.308×10^{5}	13.1472	1.525×10^{5}	23.38	172.60
−0.10	14.74	4992.80	4.643×10^{-7}	1.485×10^{5}	9.0884	1.803×10^{5}	24.00	174.60
0.00	0.00	4691.80	5.685×10^{-7}	1.708×10^{5}	7.0124	2.081×10^{5}	24.25	176.60

NOTE.—Table 9 is also available in machine-readable form in the electronic edition of the *Astrophysical Journal Supplement*.

TABLE 10

MODEL F: STRAY LIGHT FRACTION: 0.55

$\log(\tau_{500})$	Height (km)	Temp. (K)	Density (g cm^{-3})	Gas Press. (dyn cm^{-2})	Electron Press. (dyn cm^{-2})	$v_{\rm los}$ (cm s^{-1})	B (G)	γ (deg)
−5.90	2887.00	11944.40	3.491×10^{-14}	0.1848	9.232×10^{-2}	4.024×10^{5}	984.64	87.96
−5.80	2538.62	11448.30	3.428×10^{-14}	0.2012	0.1004	3.456×10^{5}	986.70	87.59
−5.70	2275.29	10944.60	1.762×10^{-13}	0.2403	0.1168	2.940×10^{5}	988.58	87.63
−5.60	2184.87	10423.50	2.244×10^{-13}	0.2877	0.1379	2.473×10^{5}	990.28	87.38
−5.50	2094.94	9903.80	2.880×10^{-13}	0.3491	0.1664	2.053×10^{5}	991.79	86.78
−5.40	2007.69	9393.20	3.708×10^{-13}	0.4256	0.2026	1.678×10^{5}	993.13	86.17
−5.30	1923.83	8889.60	4.801×10^{-13}	0.5205	0.2472	1.414×10^{5}	994.07	85.54
−5.20	1844.17	8395.90	6.273×10^{-13}	0.6378	0.3005	1.182×10^{5}	994.01	84.99
−5.10	1768.41	7954.40	8.335×10^{-13}	0.7825	0.3580	9.530×10^{4}	993.83	84.49
−5.00	1694.63	7534.90	1.198×10^{-12}	0.9809	0.4030	6.950×10^{4}	993.42	83.97
−4.90	1617.34	7176.80	1.947×10^{-12}	1.3038	0.4089	5.224×10^{4}	992.99	83.42
−4.80	1528.81	6901.70	3.517×10^{-12}	1.9525	0.3982	3.753×10^{4}	992.43	82.86
−4.70	1423.25	6625.60	7.398×10^{-12}	3.5071	0.3681	2.518×10^{4}	991.64	82.28
−4.60	1295.24	6291.30	1.961×10^{-11}	8.2069	0.3058	1.501×10^{4}	990.73	81.68
−4.50	1156.47	5986.60	5.659×10^{-11}	21.9497	0.2575	6.854×10^{3}	989.79	81.06
−4.40	1032.92	5708.90	1.433×10^{-10}	52.6051	0.2030	4.842×10^{3}	988.62	80.42
−4.30	935.30	5490.20	3.040×10^{-10}	1.070×10^{2}	0.1642	4.330×10^{3}	987.33	79.76
−4.20	861.42	5336.90	5.471×10^{-10}	1.871×10^{2}	0.1449	4.027×10^{3}	985.91	79.08
−4.10	804.73	5249.90	8.653×10^{-10}	2.910×10^{2}	0.1452	3.888×10^{3}	984.36	78.38
−4.00	760.36	5214.00	1.239×10^{-9}	4.138×10^{2}	0.1607	3.868×10^{3}	982.69	77.90
−3.90	724.55	5208.70	1.652×10^{-9}	5.513×10^{2}	0.1871	3.918×10^{3}	980.79	77.93
−3.80	694.33	5209.60	2.105×10^{-9}	7.026×10^{2}	0.2163	3.995×10^{3}	978.86	77.89
−3.70	667.47	5199.60	2.618×10^{-9}	8.719×10^{2}	0.2401	4.051×10^{3}	976.81	77.63
−3.60	642.56	5186.30	3.206×10^{-9}	1.065×10^{3}	0.2628	3.120×10^{3}	974.53	76.73
−3.50	619.10	5179.40	3.874×10^{-9}	1.285×10^{3}	0.2908	2.278×10^{3}	972.22	75.83
−3.40	596.97	5190.60	4.606×10^{-9}	1.531×10^{3}	0.3335	2.579×10^{3}	969.69	74.90
−3.30	575.92	5189.80	5.442×10^{-9}	1.809×10^{3}	0.3706	2.375×10^{3}	967.03	73.97
−3.20	555.32	5159.00	6.462×10^{-9}	2.135×10^{3}	0.3874	2.362×10^{3}	964.24	73.02
−3.10	534.99	5155.00	7.585×10^{-9}	2.504×10^{3}	0.4283	1.377×10^{3}	961.33	72.06
−3.00	515.06	5133.30	8.919×10^{-9}	2.932×10^{3}	0.4588	3.616×10^{-1}	958.30	71.08
−2.90	495.37	5110.60	1.046×10^{-8}	3.424×10^{3}	0.4929	-1.747×10^{3}	955.14	70.09
−2.80	475.94	5087.20	1.223×10^{-8}	3.985×10^{3}	0.5314	-3.814×10^{3}	951.84	69.09
−2.70	456.81	5074.10	1.420×10^{-8}	4.614×10^{3}	0.5830	-6.134×10^{3}	948.43	68.07
−2.60	437.99	5052.60	1.648×10^{-8}	5.331×10^{3}	0.6342	-9.130×10^{3}	944.78	67.02
−2.50	419.45	5031.80	1.905×10^{-8}	6.138×10^{3}	0.6925	-1.240×10^{4}	941.11	65.71
−2.40	401.20	5006.90	2.199×10^{-8}	7.050×10^{3}	0.7549	-1.579×10^{4}	937.21	64.37
−2.30	383.23	4982.60	2.530×10^{-8}	8.074×10^{3}	0.8254	-1.917×10^{4}	933.29	63.01
−2.20	365.51	4974.00	2.890×10^{-8}	9.204×10^{3}	0.9147	-2.203×10^{4}	929.14	61.63
−2.10	347.90	4978.30	3.282×10^{-8}	1.046×10^{4}	1.0234	-2.438×10^{4}	924.86	60.30
−2.00	330.33	4988.20	3.718×10^{-8}	1.188×10^{4}	1.1493	-2.588×10^{4}	920.45	59.20
−1.90	312.77	4998.30	4.212×10^{-8}	1.348×10^{4}	1.2904	-2.729×10^{4}	915.92	58.07
−1.80	295.35	5025.40	4.811×10^{-8}	1.548×10^{4}	1.4843	-2.857×10^{4}	911.27	56.93
−1.70	278.23	5054.40	5.478×10^{-8}	1.773×10^{4}	1.7058	-2.865×10^{4}	906.48	55.77
−1.60	261.29	5087.00	6.217×10^{-8}	2.025×10^{4}	1.9626	-2.876×10^{4}	901.57	54.59
−1.50	244.49	5133.10	7.022×10^{-8}	2.308×10^{4}	2.2825	-2.781×10^{4}	896.43	53.39
−1.40	227.76	5178.70	7.921×10^{-8}	2.627×10^{4}	2.6528	-2.653×10^{4}	891.27	52.52
−1.30	211.09	5232.90	8.907×10^{-8}	2.985×10^{4}	3.1096	-2.277×10^{4}	885.98	52.10
−1.20	194.49	5289.20	9.998×10^{-8}	3.387×10^{4}	3.6567	-1.696×10^{4}	880.46	51.26
−1.10	177.80	5346.00	1.106×10^{-7}	3.785×10^{4}	4.2622	-9.418×10^{3}	874.82	50.03
−1.00	160.84	5404.50	1.224×10^{-7}	4.238×10^{4}	4.9986	3.064×10^{1}	869.15	48.80
−0.90	143.75	5467.70	1.356×10^{-7}	4.749×10^{4}	5.9194	1.114×10^{4}	863.26	47.55
−0.80	126.64	5531.30	1.503×10^{-7}	5.325×10^{4}	7.0391	2.430×10^{4}	857.08	46.29
−0.70	109.61	5603.00	1.663×10^{-7}	5.967×10^{4}	8.4949	4.101×10^{4}	849.83	45.02
−0.60	92.80	5678.50	1.837×10^{-7}	6.681×10^{4}	10.3447	6.103×10^{4}	842.40	43.74
−0.50	76.30	5759.30	2.025×10^{-7}	7.469×10^{4}	12.7396	8.888×10^{4}	834.79	42.45
−0.40	60.20	5841.80	2.227×10^{-7}	8.333×10^{4}	15.7650	1.257×10^{5}	827.00	41.14
−0.30	44.52	5924.90	2.444×10^{-7}	9.276×10^{4}	19.5468	1.671×10^{5}	819.02	39.87
−0.20	29.27	6008.00	2.689×10^{-7}	1.035×10^{5}	24.3004	2.110×10^{5}	818.26	38.91
−0.10	14.48	6092.00	2.944×10^{-7}	1.149×10^{5}	30.1946	2.591×10^{5}	811.29	37.94
0.00	0.00	6171.30	3.207×10^{-7}	1.268×10^{5}	37.0583	3.121×10^{5}	804.19	36.97

NOTE.—Table 10 is also available in machine-readable form in the electronic edition of the *Astrophysical Journal Supplement*.

TABLE 11

MODEL G: STRAY LIGHT FRACTION: 0.29

$\log(\tau_{500})$	Height (km)	Temp. (K)	Density (g cm^{-3})	Gas Press. (dyn cm^{-2})	Electron Press. (dyn cm^{-2})	$v_{\rm los}$ (cm s^{-1})	B (G)	γ (deg)
−5.90	2203.49	7967.00	3.917×10^{-13}	0.3751	0.1752	-3.033×10^{5}	1636.40	164.73
−5.80	2171.55	8736.90	3.752×10^{-13}	0.3997	0.1898	-2.927×10^{5}	1548.70	165.85
−5.70	2132.43	9487.90	3.707×10^{-13}	0.4298	0.2046	-2.802×10^{5}	1469.60	166.36
−5.60	2083.86	10134.00	3.824×10^{-13}	0.4745	0.2263	-2.658×10^{5}	1398.80	165.79
−5.50	2026.06	10618.60	4.062×10^{-13}	0.5302	0.2540	-2.498×10^{5}	1335.80	165.37
−5.40	1959.82	10857.20	4.515×10^{-13}	0.6045	0.2905	-2.322×10^{5}	1280.30	165.12
−5.30	1889.69	10082.50	5.651×10^{-13}	0.6970	0.3322	-2.134×10^{5}	1231.80	165.02
−5.20	1818.31	9811.40	6.776×10^{-13}	0.8127	0.3869	-1.934×10^{5}	1215.80	165.07
−5.10	1745.61	9375.00	8.351×10^{-13}	0.9557	0.4543	-1.684×10^{5}	1239.30	165.26
−5.00	1674.45	8798.40	1.058×10^{-12}	1.1305	0.5345	-1.392×10^{5}	1270.20	165.54
−4.90	1607.13	8138.30	1.403×10^{-12}	1.3464	0.6151	-1.088×10^{5}	1306.90	165.92
−4.80	1540.99	7552.50	2.081×10^{-12}	1.6373	0.6309	-7.992×10^{4}	1347.80	166.34
−4.70	1457.75	6907.70	4.354×10^{-12}	2.3807	0.4549	-5.532×10^{4}	1391.10	166.80
−4.60	1321.45	6282.70	1.509×10^{-11}	6.3313	0.2622	-3.772×10^{4}	1435.30	167.25
−4.50	1143.00	5789.00	6.636×10^{-11}	24.7680	0.1694	-2.901×10^{4}	1478.60	167.69
−4.40	990.45	5425.00	2.124×10^{-10}	73.9140	0.1133	-1.134×10^{4}	1519.50	168.08
−4.30	887.79	5191.30	4.802×10^{-10}	1.597×10^{2}	8.857×10^{-2}	1.165×10^{4}	1556.20	168.40
−4.20	818.58	5070.40	8.497×10^{-10}	2.760×10^{2}	8.668×10^{-2}	3.414×10^{4}	1587.00	168.33
−4.10	769.37	5023.40	1.278×10^{-9}	4.112×10^{2}	9.790×10^{-2}	3.960×10^{4}	1610.50	168.12
−4.00	731.98	5021.10	1.734×10^{-9}	5.576×10^{2}	0.1181	4.794×10^{4}	1624.80	167.87
−3.90	701.63	5033.60	2.212×10^{-9}	7.130×10^{2}	0.1427	6.926×10^{4}	1628.40	167.57
−3.80	675.35	5035.80	2.733×10^{-9}	8.813×10^{2}	0.1650	1.079×10^{5}	1619.50	167.23
−3.70	651.44	5032.80	3.313×10^{-9}	1.068×10^{3}	0.1867	1.332×10^{5}	1597.20	166.85
−3.60	629.04	5022.60	3.973×10^{-9}	1.278×10^{3}	0.2071	1.492×10^{5}	1562.80	166.43
−3.50	607.62	4999.20	4.743×10^{-9}	1.519×10^{3}	0.2243	1.636×10^{5}	1518.60	165.97
−3.40	586.91	4968.20	5.639×10^{-9}	1.794×10^{3}	0.2410	1.762×10^{5}	1466.50	165.46
−3.30	566.82	4933.00	6.670×10^{-9}	2.107×10^{3}	0.2591	1.868×10^{5}	1408.60	164.91
−3.20	547.54	4963.80	7.761×10^{-9}	2.467×10^{3}	0.3063	1.954×10^{5}	1347.10	164.30
−3.10	529.21	4998.30	8.947×10^{-9}	2.864×10^{3}	0.3614	2.017×10^{5}	1284.00	163.64
−3.00	511.39	5022.90	1.015×10^{-8}	3.266×10^{3}	0.4147	2.056×10^{5}	1221.30	162.93
−2.90	493.69	5027.10	1.159×10^{-8}	3.731×10^{3}	0.4627	2.154×10^{5}	1222.70	162.17
−2.80	476.04	5013.40	1.330×10^{-8}	4.270×10^{3}	0.5055	2.272×10^{5}	1238.30	161.35
−2.70	458.49	4965.10	1.543×10^{-8}	4.907×10^{3}	0.5351	2.324×10^{5}	1253.70	160.47
−2.60	441.16	4918.00	1.784×10^{-8}	5.620×10^{3}	0.5725	2.314×10^{5}	1268.90	159.57
−2.50	424.13	4879.00	2.051×10^{-8}	6.409×10^{3}	0.6197	2.246×10^{5}	1283.60	158.65
−2.40	407.23	4887.30	2.317×10^{-8}	7.252×10^{3}	0.6938	1.710×10^{5}	1297.90	157.68
−2.30	390.38	4861.00	2.648×10^{-8}	8.244×10^{3}	0.7592	1.540×10^{5}	1311.60	156.67
−2.20	373.71	4843.80	3.015×10^{-8}	9.352×10^{3}	0.8354	1.336×10^{5}	1324.60	155.61
−2.10	357.11	4837.90	3.419×10^{-8}	1.059×10^{4}	0.9257	1.095×10^{5}	1336.70	154.52
−2.00	340.49	4842.80	3.865×10^{-8}	1.199×10^{4}	1.0327	8.285×10^{4}	1348.20	153.71
−1.90	323.76	4859.40	4.355×10^{-8}	1.355×10^{4}	1.1612	5.454×10^{4}	1358.90	153.71
−1.80	307.01	4896.00	4.952×10^{-8}	1.553×10^{4}	1.3406	2.567×10^{4}	1369.00	153.71
−1.70	290.36	4943.90	5.605×10^{-8}	1.775×10^{4}	1.5584	-2.700×10^{3}	1378.50	153.71
−1.60	273.73	5000.90	6.322×10^{-8}	2.025×10^{4}	1.8232	-2.952×10^{4}	1405.60	153.71
−1.50	256.96	5023.20	7.090×10^{-8}	2.281×10^{4}	2.0525	-4.633×10^{4}	1510.40	153.71
−1.40	240.06	5080.50	8.001×10^{-8}	2.603×10^{4}	2.4058	-7.430×10^{4}	1619.50	153.71
−1.30	223.17	5151.00	8.989×10^{-8}	2.965×10^{4}	2.8537	-9.014×10^{4}	1697.00	153.71
−1.20	206.32	5221.60	1.009×10^{-7}	3.372×10^{4}	3.3930	-1.002×10^{5}	1697.00	153.71
−1.10	189.53	5285.30	1.132×10^{-7}	3.831×10^{4}	4.0163	-1.034×10^{5}	1697.00	153.71
−1.00	172.64	5336.10	1.255×10^{-7}	4.289×10^{4}	4.6462	-9.879×10^{4}	1697.00	153.71
−0.90	155.47	5371.90	1.401×10^{-7}	4.820×10^{4}	5.3048	-8.520×10^{4}	1697.00	153.71
−0.80	138.06	5404.00	1.568×10^{-7}	5.427×10^{4}	6.0405	-6.162×10^{4}	1697.00	153.71
−0.70	120.50	5460.80	1.744×10^{-7}	6.099×10^{4}	7.0810	-2.698×10^{4}	1697.00	153.71
−0.60	102.91	5535.70	1.931×10^{-7}	6.846×10^{4}	8.5147	5.288×10^{3}	1697.00	153.71
−0.50	85.47	5619.90	2.133×10^{-7}	7.679×10^{4}	10.4210	3.410×10^{4}	1697.00	153.71
−0.40	68.24	5684.20	2.367×10^{-7}	8.616×10^{4}	12.4450	4.743×10^{4}	1697.00	153.71
−0.30	51.17	5750.90	2.623×10^{-7}	9.660×10^{4}	14.9400	6.077×10^{4}	1697.00	153.71
−0.20	34.06	5768.50	2.942×10^{-7}	1.087×10^{5}	16.6455	7.410×10^{4}	1697.00	153.71
−0.10	16.82	5823.50	3.273×10^{-7}	1.221×10^{5}	19.6485	8.743×10^{4}	1697.00	153.71
0.00	0.00	5915.80	3.637×10^{-7}	1.378×10^{5}	24.7673	1.008×10^{5}	1697.00	153.71

NOTE.—Table 11 is also available in machine-readable form in the electronic edition of the *Astrophysical Journal Supplement*.

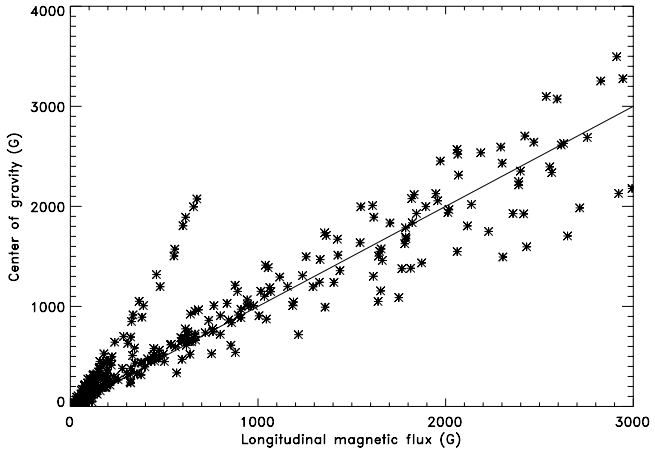

FIG. 17.—Scatter plot of the center-of-gravity prediction vs. the actual magnetic flux corresponding to synthetic profiles.

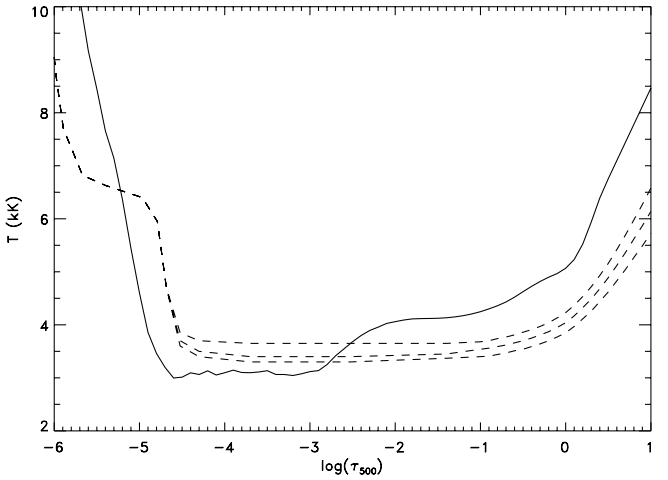

FIG. 18.—Comparison between average umbral model (*solid line*) and models E, M, and L of Maltby et al. (*dashed line*, from cool to hot).

reduction of Stokes V signal, and that might lead to a decrease in the measured center of gravity. Stokes V cancellation might also arise from the self-reversals in point F.

The fits to the umbral profiles A and B (Figs. 3 and 5) show some residual wavelength shift in Stokes I that is not present in the polarization profiles. This is because the stray light profiles are shifted with respect to the umbral spectra. The inversion code used here does not adjust the wavelength shift of the stray light profile. Thus, the velocities obtained correspond to the magnetic atmosphere.

The height dependence of the umbral magnetic field is rather flat, especially in the photosphere. The slope becomes larger as one moves radially away from the center of the sunspot. Typical photospheric umbral models have a field gradient of roughly ~ -3 G km^{-1}. However, those are generally determined from low-resolution observations and refer to the umbra as a whole. When seen in high resolution, it is possible to have individual pixels exhibiting a different gradient, as we see here, especially when the sunspot is irregular.

The penumbral velocity stratifications (points C and D) yield strong redshifts at photospheric heights and blueshifts in the chromosphere. Since these points are observed on the limb-side penumbra, those velocities correspond to the Evershed flow (inverse flow in the chromosphere).

Point D corresponds to a location where there is virtually no flux according to the photospheric magnetogram, but there is some signal in the chromospheric lines. The denomination of "canopy" may not be very precise in the context that this word is traditionally employed, given that the two sunspots have the same polarity. In any case, as seen in the inversion results, this is a region where there is significantly more flux present in the higher layers.

Figures 18 and 19 show how the models derived in this work compare to some previously published umbral and quiet-Sun models. The sunspot umbra has a hotter photosphere but, while the Maltby et al. (1986) atmosphere has a flat temperature plateau, the temperature in points A and B decreases outward.

The network and facula analyzed here have a considerably hotter chromosphere than those of Vernazza et al. (1981) and Gingerich et al. (1971). This is not surprising since magnetic elements usually exhibit enhanced brightness in the core of chromospheric lines, probably due to the propagation of waves inside such elements.

TABLE 12

COMPARISON OF LONGITUDINAL MAGNETIC FLUX TO CENTER-OF-GRAVITY METHOD

Point	Center of Gravity (G)	Flux from Model (G)
A	1496.40	1418.95
B	1934.61	1946.81
C	0.06	614.18
D	425.75	972.31
E	265.06	391.33
F	146.84	409.23
G	800.44	795.52

4. CONCLUSIONS

The fits to the observed Stokes spectra are generally very good, indicating that these profiles can be well represented by

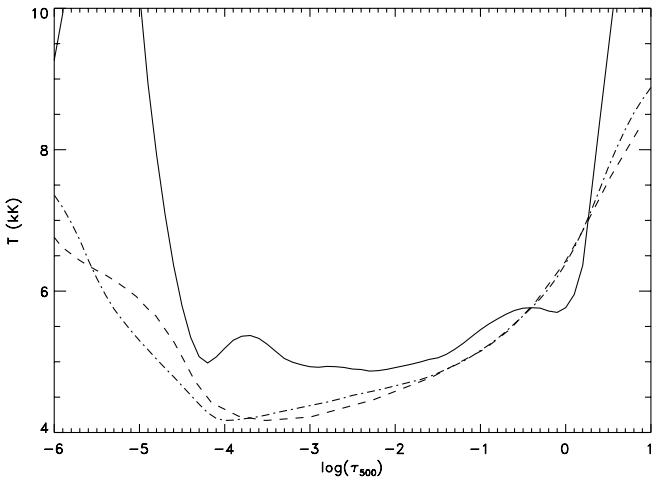

FIG. 19.—Comparison between average network and facula model (*solid line*), model C of Vernazza et al. (1981, *dashed line*), and the Harvard Smithsonian Reference Atmosphere of Gingerich et al. (1971, *dash-dotted line*).

one-component model atmospheres. This is probably due to the spatial resolution attained in the observations, which allows one to separate partially the hot and cool components in the sunspot. Some of the Stokes profiles are very asymmetric, which sets constrains on the velocity and magnetic field gradients retrieved.

The derivation of semiempirical models may be improved in the future by obtaining a larger number of observations, ideally at multiple spectral ranges. The fitting of many spectral lines from several ions would complicate the calculations considerably, but it would be very helpful in setting stronger constrains and therefore reducing the error bars.

The author is grateful to the staff at the Sacramento Peak observatory (Sunspot, NM) of the National Solar Observatory for their enthusiastic support of these observations and the SPINOR project in general. Thanks are also due to the anonymous referee who helped improve the original manuscript.

REFERENCES

Bellot Rubio, L. R., Ruiz Cobo, B., & Collados, M. 1997, ApJ, 478, L45
Collados, M., Martinez Pillet, V., Ruiz Cobo, B., del Toro Iniesta, J. C., & Vazquez, M. 1994, A&A, 291, 622
Fontenla, J. M., Avrett, E. H., & Loeser, R. 1990, ApJ, 355, 700
Gingerich, O., Noyes, R. W., Kalkofen, W., & Cuny, Y. 1971, Sol. Phys., 18, 347
Maltby, P., Avrett, E. H., Carlsson, M., Kjeldseth-Moe, O., Kurucz, R. L., & Loeser, R. 1986, ApJ, 306, 284
Rees, D. E., & Semel, M. D. 1979, A&A, 74, 1
Ren, D., Hegwer, S. L., Rimmele, T., Didkovsky, L. V., & Goode, P. R. 2003, Proc. SPIE, 4853, 593
Scharmer, G., & Carlsson, M. 1985, J. Comput. Phys., 59, 56
Shchukina, N., & Trujillo Bueno, J. 2001, ApJ, 550, 970
Socas-Navarro, H., Elmore, D., Pietarila, A., Darnell, A., Lites, B., & Tomczyk, S. 2006, Sol. Phys., 235, 55
Socas-Navarro, H., Trujillo Bueno, J., & Ruiz Cobo, B. 2000a, ApJ, 544, 1141
———. 2000b, ApJ, 530, 977
Vernazza, J. E., Avrett, E. H., & Loeser, R. 1981, ApJS, 45, 635